



## **A multiscale analytical-numerical method for the coupled heat and mass transfer in the extended meniscus region considering thin-film evaporation in microchannels**

**Mostafazade Abolmaali, Ali; Bayat, Mohamad; Hattel, Jesper**

*Published in:*  
International Journal of Heat and Mass Transfer

*Link to article, DOI:*  
[10.1016/j.ijheatmasstransfer.2023.125145](https://doi.org/10.1016/j.ijheatmasstransfer.2023.125145)

*Publication date:*  
2024

*Document Version*  
Publisher's PDF, also known as Version of record

[Link back to DTU Orbit](#)

*Citation (APA):*  
Mostafazade Abolmaali, A., Bayat, M., & Hattel, J. (2024). A multiscale analytical-numerical method for the coupled heat and mass transfer in the extended meniscus region considering thin-film evaporation in microchannels. *International Journal of Heat and Mass Transfer*, 222, Article 125145.  
<https://doi.org/10.1016/j.ijheatmasstransfer.2023.125145>

---

### **General rights**

Copyright and moral rights for the publications made accessible in the public portal are retained by the authors and/or other copyright owners and it is a condition of accessing publications that users recognise and abide by the legal requirements associated with these rights.

- Users may download and print one copy of any publication from the public portal for the purpose of private study or research.
- You may not further distribute the material or use it for any profit-making activity or commercial gain
- You may freely distribute the URL identifying the publication in the public portal

If you believe that this document breaches copyright please contact us providing details, and we will remove access to the work immediately and investigate your claim.



# A multiscale analytical-numerical method for the coupled heat and mass transfer in the extended meniscus region considering thin-film evaporation in microchannels

Ali Mostafazade Abolmaali<sup>\*</sup>, Mohamad Bayat, Jesper Hattel

Department of Civil and Mechanical Engineering, Technical University of Denmark, Lyngby, Denmark

## ARTICLE INFO

### Keywords:

Thin-film  
Evaporation  
Microchannel  
Heat pipe  
Computational heat and fluid flow

## ABSTRACT

A Computational Fluid Dynamics (CFD) framework is established to investigate the microscale transport phenomena in the evaporating extended meniscus region formed in rectangular microchannels. A wide range of microchannel widths ( $W = 1$  to  $250 \mu\text{m}$ ) and wall superheats ( $\Delta T = 0.01$  to  $5.0 \text{ K}$ ) are considered. Prior to performing CFD simulations, it is first necessary to employ thin-film evaporation modeling based on an augmented Young–Laplace model and kinetic-theory based model for the evaporating mass flux across curved surfaces to find the exact shape of the liquid-vapor interface along with disjoining and capillary pressure distributions. Two widely-used methods for the determination of boundary conditions (BCs) at the beginning of the thin-film region (i.e., setting  $\delta_0 = 0$  and finding  $\delta_0$  by the far-field BC or setting  $\delta_0 = 0$  and finding  $\delta_0$  by the far-field BC), where  $\delta$  is film thickness, are thoroughly examined and the first approach is recommended because of its better convergence and ease of implementation in the thin-film evaporation model. Then, the two-dimensional domain of the extended meniscus is generated and discretized to simulate the evaporating liquid flow through the UDF programming in ANSYS Fluent. The developed framework is shown to be a simple yet powerful and practical method for accurately predicting the evaporation mass and heat fluxes from extended menisci in microchannels. The CFD simulation results indicate that the previous one-dimensional models which represent the state of the art in the literature in the field are not able to predict the rate of evaporative heat transfer from the extended meniscus in microchannels with an acceptable degree of accuracy. Based on the CFD simulations results, a multiple regression analysis is employed to establish several simple thermal resistance correlations. The correlations can be straightforwardly integrated into macroscale mathematical models of micro and miniature heat pipes for analyzing their thermal characteristics.

## 1. Introduction

Heat pipes are simple, efficient, two-phase heat transfer devices that are widely utilized in thermal management applications [1–3]. While different types of heat pipes have been designed and employed such as capillary pumped loops [4], loop heat pipes [5], miniature heat pipes [6], micro heat pipes [7], etc., their common feature is taking advantage of capillary wick structures to passively circulate the working fluid between the condenser (heat sink) and evaporator (heat source) sections. Among various capillary wick structures used by heat pipe manufacturers including sintered wick, wire mesh, axial grooved, artery wick, and composite wick, the axial grooved wick structures are well recognized for their long-distance heat transportation capability [8] and ease

of fabrication [9,10]. Therefore, the present study is mainly dealing with the evaporation heat transfer characteristics inside axial microgroove wick structures.

The study of evaporation heat transfer within microstructures is linked to the concept of thin-film evaporation. In fact, when the liquid inside a microchannel comes in contact with a heated solid wall, an extended meniscus is formed that can be broken down into three distinct regions as depicted in Fig. 1: a non-evaporating region (adsorbed film), an evaporating thin-film region (transition region), and an intrinsic meniscus (bulk region). Considering its very small thickness and therefore very low thermal resistance, the thin-film region plays a major role in transferring heat between the heated wall and the saturated vapor. The heat is conducted through the thin-film region towards the liquid-

<sup>\*</sup> Corresponding author.

E-mail address: [amoab@dtu.dk](mailto:amoab@dtu.dk) (A. Mostafazade Abolmaali).

<https://doi.org/10.1016/j.ijheatmasstransfer.2023.125145>

Received 6 October 2023; Received in revised form 29 November 2023; Accepted 23 December 2023

Available online 30 December 2023

0017-9310/© 2023 The Authors. Published by Elsevier Ltd. This is an open access article under the CC BY license (<http://creativecommons.org/licenses/by/4.0/>).

vapor interface where evaporation takes place. Previous studies have clarified that the thin-film region is under influence of both capillary pressure and disjoining pressure (the adhesion forces between the solid wall and the liquid-vapor interface) while it is just capillary forces that dominate the intrinsic meniscus. If the thin-film region is ignored, the heat transfer rate will be underestimated [11].

Derjaguin et al. [12] introduced the concept of wedging-point pressure (later known as disjoining pressure) to describe the reduction in liquid pressure in the thin-film liquid layers. One of the pioneer studies about thin-film evaporation is the work done by Wayner and Coccio [13]. They studied the heat and mass transfer close to the triple interline of an evaporating meniscus both experimentally and analytically. They put forward the existence of a thin-film region around the intrinsic meniscus to justify the high heat flux observed in the intrinsic region. It was Potash and Wayner [14] who found that liquid supply into the thin-film region results from the gradients of disjoining pressure and capillary pressure. Wayner et al. [15,16] employed an augmented Young–Laplace equation to incorporate the effects of disjoining pressure on liquid supply and evaporation suppression. They also developed a fugacity expression using the Gibbs–Duhem equations to simplify the Schrage model [17] for evaporation mass flux from a curved interface. This simplified model, known as Wayner’s model, has been shown to provide acceptable results for wall superheats up to about 5 K [18] and therefore is employed in the present work.

Stephan and Busse [19] obtained a fourth-order ordinary differential equation (ODE) for the film thickness in the micro region, considering capillary and disjoining pressures along with the one-dimensional lubrication approximation. They solved the two-dimensional stationary heat conduction equation in the macro region instead of the Navier–Stokes equations, neglecting the heat transfer due to the convection heat transfer mechanism. They concluded that the radial heat transfer coefficient will be highly overpredicted if it is assumed that the interface temperature is equal to the saturation temperature of the vapor. A similar methodology i.e., taking into account the disjoining and capillary pressures along with the lubrication approximation, was adopted by several authors to study different aspects of the thin-film evaporation inside microgrooves [18,20–29], phase change heat transfer during drop impingement [30], and numerical simulation of boiling flows [31,32]. Wang et al. [18] used the original Schrage’s model for mass transport across a liquid-vapor interface instead of the simplified Wayner’s model. They distinguished the thin-film region and the intrinsic meniscus based on the disjoining pressure variation along the meniscus and stated that the micro region accounted for more than 50 % of the total heat transfer.

Do et al. [33] developed a mathematical model to assess the

performance of flat micro heat pipes with grooved wicks and optimized heat transfer rate with respect to the width and the height of the grooves. To do so, they considered the extended meniscus formed on the heated wall and solved the fourth-order ODE to determine the film thickness and the interfacial temperature. They set the boundary conditions (BCs) at the intersection of the evaporating thin-film region and the intrinsic meniscus unlike several other research works that set the BCs at the intersection of the adsorbed film and the thin-film region [18,19,22,24,27], as shown in Fig. 1. Some other researchers have also chosen the starting point of the intrinsic meniscus for setting the BCs [21,25,33]. However, one drawback of this method is that it requires the contact angle, which is not a known parameter in most cases. Moreover, Do et al. [33] supposed that the interface temperature is constant all over the intrinsic meniscus and equals the saturation vapor temperature, which is not a realistic assumption leading to a wrong prediction of the evaporation mass flux.

Another interesting area of study in relation to wick microstructures and heat pipes is to obtain the shape of the liquid-vapor meniscus and the evaporation mass and heat fluxes inside wick pores. Ranjan et al. [34–36] employed Surface Evolver to model the free-surface shapes of the static liquid meniscus in some standard microstructures. Bolda et al. [37] and Remella and Gerner [38] made use of the volume-of-fluid (VOF) method in ANSYS Fluent to find the shape of the liquid-vapor interface and to investigate the thin-film evaporation of the liquid in the sintered wick and a single layer of a metallic wire mesh screen, respectively. While all these studies aimed to develop a framework for evaluating the evaporation characteristics of microstructures, they didn’t consider the effects of disjoining pressure, neither on the shape of the liquid layer in the thin-film region nor on the suppression of the evaporation mass flux. Neglecting the influence of disjoining pressure in those studies can be attributed to the disparity between the length scales encountered in the study of the extended meniscus evaporation, ranging from about one nanometer in the adsorbed film to hundreds of micrometers in the intrinsic meniscus. However, it has been plainly demonstrated that the disjoining pressure plays a crucial role in the spreading of the liquid layer in the thin-film region and therefore, it cannot be ignored in the thin-film evaporation analyses [39].

The literature survey indicates that although there are a lot of research studies done on the evaporative heat transfer from liquid-vapor meniscus, there is not a clear investigation on how the thin-film evaporation along with its governing physics can be coupled with CFD simulation techniques. Therefore, this paper is organized in a way that a numerical simulation framework is established which is capable of finding the extended meniscus profile and its related fluid flow and heat transfer characteristics. Accordingly, three main objectives are followed

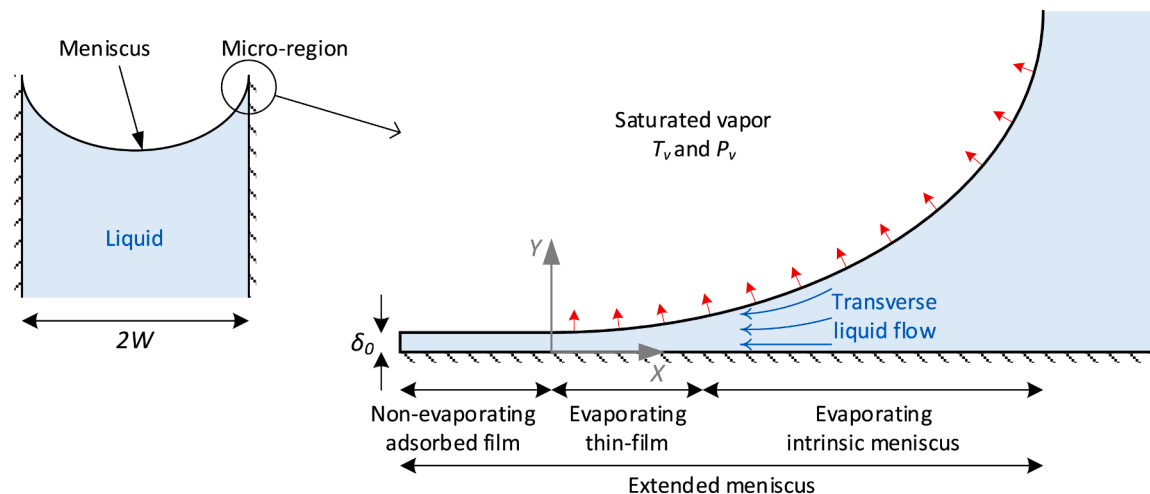


Fig. 1. Schematic representation of an extended meniscus formed in a microchannel.

in the present study. The first one is to develop a solution algorithm for the thin-film evaporation, as will be done in Section 2.1. The next goal, as explained in Section 2.2, is to build a computational framework, taking advantage of CFD simulation tools, to determine the thermohydraulic characteristics of evaporative heat transfer from extended meniscus in microchannels. After performing boundary condition, mesh, and CFD simulation validation studies in Section 3, the developed framework is used to prove its ability to obtain the exact amount of evaporation flux from an extended meniscus compared to previous studies in literature in Section 4.1. Finally, the third objective is to make use of the obtained results in order to develop simple thermal resistance correlations, which is presented in Section 4. These correlations can be straightforwardly included in macro models and hence make a junction between the micro- and macro-scale physics of heat pipes.

## 2. Theoretical model and governing equations

As mentioned in the previous section, the region near the wall, being involved in the evaporation process, can be divided into three parts i.e., a non-evaporating adsorbed film, a thin-film region and an intrinsic meniscus region. Finding the thermohydraulic characteristics of the thin-film region requires that the film profile be first calculated, as will be discussed in this section. Accordingly, based on fluid flow and heat transfer analysis in the thin-film region, a fourth-order ODE is derived, which needs to be solved by numerical methods such as the 4th order Runge–Kutta method.

To find the relative importance of the thin-film region compared to the extended meniscus in terms of the evaporation mass and heat fluxes, it is necessary to model the intrinsic meniscus region as well. However, it will be shown in Section 4.1 that the one-dimensional model developed for the thin-film region in Section 2.1 is not valid to be used for the intrinsic meniscus region. It is mainly due to the fact that the fluid flow in the bulk meniscus region is two-dimensional while the thin-film model is based on lubrication theory and therefore is only valid for a one-dimensional flow. Consequently, computational fluid dynamics (CFD) is used to find the fluid flow and heat transfer characteristics of the intrinsic meniscus region, as will be explained in Section 2.2. The workflow employed in the present work in order to investigate heat and mass transfer in the extended meniscus region of rectangular microchannels and to perform regression analysis is shown in Fig. 2.

### 2.1. Thin-film evaporation

The first step to determining the thin-film evaporation characteristics is to derive the equation of the thin-film profile, which is a fourth-order ODE. Since there are many previous studies in the literature discussing the governing equations [17–20,22–25], these equations are briefly reviewed in this section. The starting point is the augmented Young–Laplace equation [15] that relates the vapor pressure ( $P_v$ ), liquid pressure ( $P_l$ ), disjoining pressure ( $P_d$ ), and capillary pressure ( $P_c$ ) as follows:

$$P_v - P_l = P_d + P_c. \quad (1)$$

The disjoining pressure for a non-polar liquid (such as n-octane, which is the working fluid in the present study) can be related to the film thickness ( $\delta$ ) by Eq. (2), in which only the intermolecular London–Van Der Waals forces are taken into account [15]:

$$P_d = \frac{A_{Ham}}{6\pi\delta^3}, \quad (2)$$

where,  $A_{Ham}$  is known as the Hamaker constant, ranging typically from  $10^{-19}$  to  $10^{-22}$  J for different fluids. In the present study, a value of  $7.5 \times 10^{-20}$  J is chosen according to the experimental work of Hanchak et al. [24] for thin-films of n-octane on silicon wafer substrates.

Capillary pressure is calculated by Eq. (3) which is a function of surface tension ( $\sigma$ ) and interfacial curvature ( $\kappa$ ). Interfacial curvature (the inverse of the radius of curvature  $r$ ) is simply related to the first and second derivatives of the thin-film profile with respect to length  $x$  i.e.,  $\delta'$  and  $\delta''$ , respectively, as given by Eq. (4).

$$P_c = \sigma\kappa, \quad (3)$$

$$\kappa = \frac{1}{r} = \frac{\delta''}{(1 + \delta'^2)^{1.5}}. \quad (4)$$

Assuming a uniform and constant vapor pressure  $P_v$  along the interface, Eqs. (2)–(4) are substituted into Eq. (1) and differentiated with respect to  $x$  to obtain the following third-order ODE for the thin-film profile in which the liquid pressure gradient ( $dP_l/dx$ ) is an unknown parameter:

$$-\frac{dP_l}{dx} = \frac{A_{Ham}}{2\pi\delta^4}\delta' + \frac{\sigma\delta''}{(1 + \delta'^2)^{1.5}} - \frac{3\sigma\delta'\delta''^2}{(1 + \delta'^2)^{2.5}} \quad (5)$$

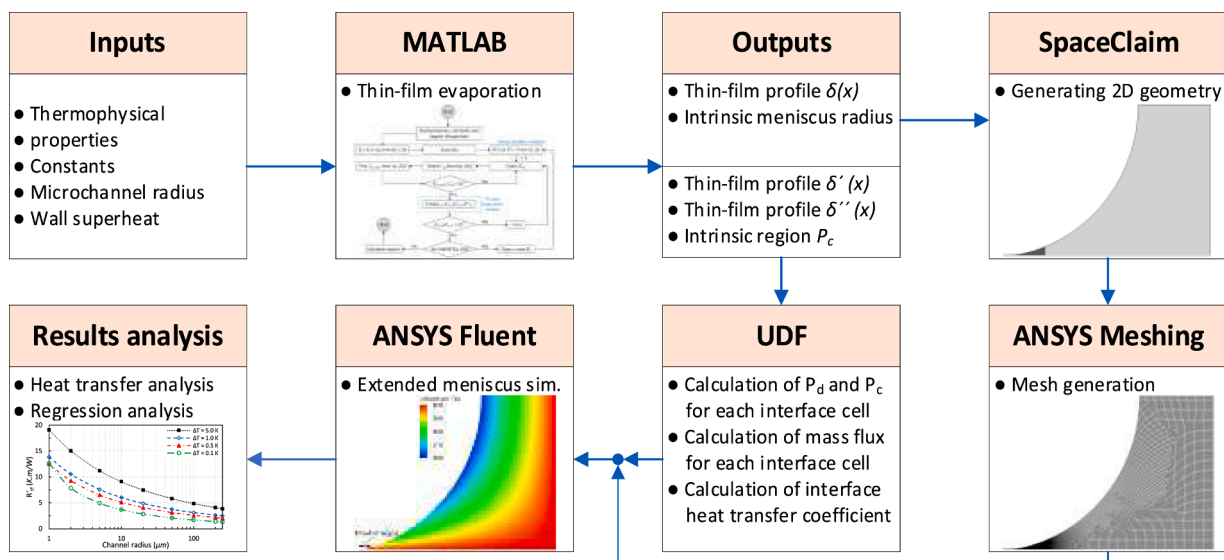


Fig. 2. The workflow developed in the present work for extended meniscus analysis.

Considering the nature of liquid flow in the thin-film region, the Navier–Stokes equations of motion can be simplified using the lubrication approximation, as suggested by several other researchers [18–20, 22–25]:

$$\frac{dP_l}{dx} = \mu_l \frac{\partial^2 u}{\partial y^2}, \quad (6)$$

where,  $u$  is the  $x$  component of velocity and  $\mu_l$  is the dynamic viscosity of liquid. Two boundary conditions required to solve Eq. (6) are a no-slip boundary condition at the wall ( $u = 0$  at  $y = 0$ ) and a no-shear boundary condition at the interface ( $\partial u / \partial y = 0$  at  $y = \delta$ ). Then, the liquid pressure gradient and the liquid mass flow rate ( $\dot{m}_l$ ) are linked together via integrating the  $u$  velocity along the thin-film thickness:

$$\dot{m}_l = \rho_l \int_0^\delta u dy = -\frac{\delta^3}{3\nu_l} \frac{dP_l}{dx} \quad (7)$$

In the above equation,  $\rho_l$  and  $\nu_l$  are liquid density and kinematic viscosity, respectively. The next step is to relate  $\dot{m}_l$  and the net evaporative mass flux ( $\dot{m}_{evp}^*$ ) of the interface as given by Eq. (8) (see Appendix A for detailed derivation of this equation).

$$\frac{d\dot{m}_l}{dx} = -\dot{m}_{evp}^* \sqrt{1 + \delta^2}. \quad (8)$$

It should be mentioned that the term  $\sqrt{1 + \delta^2}$  in Eq. (8) considers the effect of the variable slope of the thin-film profile, which was neglected in previous studies [15,17–22,24,25,27–29,33,40–46]. Finally, combining Eqs. (5) and (7), differentiating with respect to  $x$ , and then substituting the right hand side of Eq. (8) for  $d\dot{m}_l/dx$ , the following fourth-order ODE for thin-film thickness is obtained:

$$\frac{d}{dx} \left( \frac{A_{Ham} \delta'}{2\pi\delta} - \frac{\sigma \delta^3 \delta''}{(1 + \delta^2)^{1.5}} + \frac{3\sigma \delta^3 \delta' \delta''}{(1 + \delta^2)^{2.5}} \right) = 3\nu_l \dot{m}_{evp}^* \sqrt{1 + \delta^2}. \quad (9)$$

The next step is the calculation of the evaporation mass flux ( $\dot{m}_{evp}^*$ ). The most widely used approach is the one proposed by Schrage [47] for evaporation at an interface, which can be expressed as follows [48]:

$$\dot{m}_{evp}^* = \frac{2\hat{\sigma}}{2 - \hat{\sigma}} \sqrt{\frac{\bar{M}}{2\pi\bar{R}}} \left( \frac{P_{v,e}}{\sqrt{T_{int}}} - \frac{P_v}{\sqrt{T_v}} \right), \quad (10)$$

where,  $\hat{\sigma}$ ,  $\bar{M}$ ,  $\bar{R}$ ,  $P_{v,e}$ ,  $T_{int}$ ,  $P_v$ , and  $T_v$  are accommodation coefficient, molecular weight, universal gas constant, equilibrium vapor pressure, the temperature of liquid at interface, vapor pressure, and vapor temperature, respectively. While in the case of a flat interface, equilibrium vapor pressure ( $P_{v,e}$ ) is simply equal to the saturation pressure at  $T_{int}$  ( $P_{sat}$ ), it is not equal to  $P_{sat}$  when the interface is curved due to the effects of capillary and disjoining pressures. Wayner et al. [15,16] simplified Eq. (10) by making use of the Gibbs–Duhem equations, thermal equilibrium approximation over the interface, and neglecting the vapor density in comparison to the liquid density, and developed the following expression for evaporation mass flux over curved interfaces, which has been widely used by previous researchers [17,20,21,25,33,46,49]:

$$\dot{m}_{evp}^* = \frac{2\hat{\sigma}}{2 - \hat{\sigma}} \sqrt{\frac{\bar{M}}{2\pi\bar{R}T_{int}}} \left[ \frac{P_v \bar{M} h_{fg}}{\bar{R}T_v T_{int}} (T_{int} - T_v) - \frac{P_v \bar{M}}{\rho_l \bar{R}T_{int}} (P_d + P_c) \right]. \quad (11)$$

In the above formula,  $h_{fg}$  is the latent heat of evaporation and  $\rho_l$  is the liquid density. It has been shown that Eq. (11) is sufficiently accurate for up to 5 K superheat ( $\Delta T = T_{wall} - T_v$ ) [18], which is the same as the superheat range adopted in the present study. Now, substituting Eq. (11) into Eq. (9) and considering the definitions of disjoining and capillary pressures (Eqs. (2)–(4)), the desired fourth-order ODE for the thin-film profile is obtained.

It should be noted that the interface temperature  $T_{int}$  in Eq. (11) needs to be determined. While some previous studies used the Clausius–Clapeyron equation [22,45,50–52], some others applied the energy balance method [18,20,24,25,27,33]. However, Ahmed and Pandey [46] applied both methods and concluded that the interface temperature calculated based on the energy balance method agrees well with experimental data. Therefore, in the present study, the energy balance method given by Eq. (12) is used to find the interface temperature:

$$T_{int} = T_{wall} - \frac{\dot{m}_{evp}^* h_{fg}}{k_l} \delta, \quad (12)$$

where,  $T_{wall}$  is the solid wall temperature and  $k_l$  is the liquid thermal conductivity.

### 2.1.1. Boundary conditions

Since Eq. (9) is a fourth-order ODE, it requires four boundary conditions (BCs) at the beginning of the thin-film region ( $x = 0$ ) namely,  $\delta_0$ ,  $\delta'_0$ ,  $\delta''_0$ , and  $\delta'''_0$ . The initial thickness of the thin-film region ( $\delta_0$ ), which is equal to the adsorbed film thickness as well, can be obtained by setting  $\dot{m}_{evp}^* = 0$  and  $T_{int} = T_{wall}$  in Eq. (11), and assuming a zero curvature for the adsorbed film ( $P_{c,0} = 0$ ). Consequently, the following relation is obtained for the initial film thickness:

$$\delta_0 = \left( \frac{A_{Ham} T_v}{6\pi\rho_l h_{fg} (T_{wall} - T_v)} \right)^{1/3}. \quad (13)$$

However, as mentioned by previous studies, if the thin-film thickness at zero is set exactly equal to  $\delta_0$ , the evaporation mass flux will be zero all along the interface and a trivial solution i.e., a flat profile, will be obtained [18]. Thus, to tackle this issue, it is suggested that one should multiply the value obtained by Eq. (13) by a factor slightly larger than unity [17,18,24]. Although the closer to unity this factor is, the more accurate solution is obtained, it is elucidated in Section 3.1 that a factor of 1.2 is sufficient to bring about both accuracy and reasonable computational time.

The next two BCs are the first and second derivatives of the thin-film thickness at the beginning of the thin-film region i.e.,  $\delta'_0$  and  $\delta''_0$ , respectively. Some researchers set  $\delta''_0 = 0$  and found  $\delta'_0$  by a far-field BC [28,43,53] while some others put  $\delta'_0 = 0$  and determine  $\delta''_0$  using a far-field BC [18,44,45]. Since, to the best of the authors' knowledge, there is no comparison between these two methods in the open literature, a survey is provided in Section 3.1 to illustrate how these two methods affect the results. All in all, in the present study, the first method is utilized in which  $\delta''_0 = 0$ , and  $\delta'_0$  is found through an iterative calculation algorithm so that the following far-field BC is satisfied [17] (see Appendix B for detailed derivation of this equation):

$$W = \delta_{end} + \frac{R_{end}}{(1 + \delta_{end}^2)^{0.5}} = \delta_{end} + \frac{1 + \delta_{end}'^2}{\delta_{end}'}, \quad (14)$$

in which  $W$  is half width of the microchannel as depicted in Fig. 1 and subscript *end* refers to the end point of the thin-film region. Therefore,  $R_{end}$  indicates the radius of curvature at the end of the thin-film region. The last BC is  $\delta'''_0$  that can be obtained by substituting the other three BCs into Eq. (5) while setting  $dP_l/dx = 0$ .

### 2.1.2. Thin-film length criterion

Despite abundant research works published about the thin-film evaporation characteristics, determining the location where the actual thin-film region ends and therefore, where the intrinsic region starts, still seems to be a matter of conflict. Some researchers considered a constant value for the thin-film region length [19,22] while others set a pressure-dependent criterion to determine the end point of the thin-film region [18,46]. For instance, in the work done by Wang et al. [18], the



thin-film region ends where the disjoining pressure drops to 1/5000th of  $P_{d,0}$  (disjoining pressure at the beginning of the thin-film region). Moreover, several researchers extended the applicability of the thin-film governing equations to the intrinsic region and set the conditions at the end of the extended meniscus (i.e.,  $\delta \rightarrow \infty$  when  $\delta \rightarrow W$ ) as a criterion for checking solution convergence [27,29]. However, it will be shown in Section 4.1 that the governing equations in the thin-film region are not applicable to the intrinsic region.

A good criterion for determination of the thin-film length  $x_{tf}$  should be able to give a rational procedure for determining  $x_{tf}$  where two conditions are met simultaneously i.e., a negligible disjoining pressure and an insignificant capillary pressure gradient. The latter ensures that after the end point ( $x \geq x_{tf}$ ) the capillary pressure is not going to change considerably which means that the radius of curvature has almost reached its asymptotic value. Accordingly, it is found that the criterion given by Eq. (15) will be a better choice to meet the two requirements of a good criterion mentioned above. The superior performance of the suggested criterion compared to the old one i.e., 1/5000th of  $P_{d,0}$  criterion, will be discussed in Section 4.2.

$$\frac{P_{d,end}}{P_{c,end}} < 10^{-3}. \quad (15)$$

In the above inequality,  $P_{d,end}$  and  $P_{c,end}$  are disjoining pressure and capillary pressure at the end of the thin-film region, respectively.

### 2.1.3. Solution algorithm

To make it clear how the thin-film evaporation model works, the solution algorithm is depicted in Fig. 3. The solution starts with setting fluid properties, constants, and degree of superheat as given in Table 1. Then, the initial thickness of the film is calculated by multiplying Eq. (13) by a factor of 1.2. Next, the first derivative of the thin-film profile at zero ( $\delta'_0$ ), which is generally a value between 0 and 0.01, is estimated, and then, the third derivative of the profile at zero ( $\delta'''_0$ ) is found by Eq. (5), while the second derivative is set at zero ( $\delta''_0 = 0$ ). Afterwards, the interface temperature needs to be determined by an iterative process using Eqs. (11) and (12). Now, the thin-film profile and its derivatives for the next point ( $i + 1$ ) can be evaluated by solving Eq. (9) using a

**Table 1**

Constants and properties of working liquid (n-octane) at saturation temperature ( $T_v = 298.15$  K).

Parameter	Value	Unit
Hamaker constant ( $A_{Ham}$ )	$7.5 \times 10^{-20}$	J
Accommodation coeff. ( $\bar{\alpha}$ )	1	–
Molecular weight ( $\bar{M}$ )	114.23	kg/kmole
Vapor pressure ( $P_v$ )	1874	Pa
Liquid density ( $\rho_l$ )	698.5	kg/m <sup>3</sup>
Liquid specific heat ( $c_{p,l}$ )	2228	J/kg.K
Viscosity ( $\mu$ )	$5.11 \times 10^{-4}$	Pa.s
Thermal conductivity ( $k_l$ )	0.1246	W/m.K
Surface tension ( $\sigma$ )	$2.114 \times 10^{-2}$	N/m
Latent heat ( $h_{fg}$ )	$3.6342 \times 10^5$	J/kg

numerical method like 4th order Runge–Kutta. The length step used in the present study is 1 nm ( $10^{-9}$  m). Subsequently, the thin-film length criterion, Eq. (15), is checked to determine whether it is the end point of the thin-film region. If this criterion is not satisfied, the solution needs to be moved another step forward; otherwise, the far-field BC, Eq. (14), should be examined. In cases where the far-field BC is not fulfilled, the initial value estimated for  $\delta'_0$  must be modified using searching algorithms such as the dichotomy method. The solution converges when the far-field BC is satisfied.

### 2.2. Extended meniscus evaporation

There are two main motivations behind implementing CFD in the present study. The first one is to find the relative importance of the thin-film region compared to the extended meniscus region in terms of evaporation mass and heat fluxes for a wide range of microchannel widths (from 2  $\mu$ m to 500  $\mu$ m) and wall superheat (from 0.01 K to 5.0 K). The next one is using multiple regression analysis in MATLAB to derive correlations for heat transfer characteristics of the extended meniscus as a function of geometrical parameters and wall superheat. The correlations can be used by a macro model characterizing fluid flow and heat transfer in a microgroove wick structure such as those found in micro and miniature heat pipes. Hence, a two-dimensional simulation

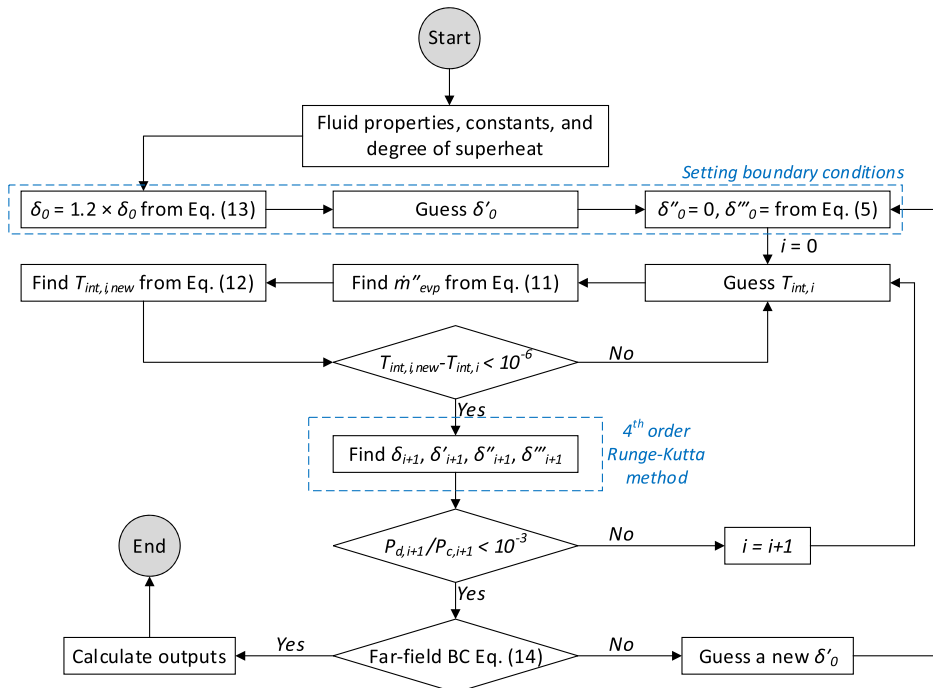


**Fig. 3.** Solution algorithm for the thin-film evaporation model.

framework is established based on user-defined functions (UDFs) in ANSYS Fluent as described in the following subsections. It should be noted that the term *extended meniscus* herein refers to the whole meniscus incorporated in the evaporation process i.e., the thin-film region and the intrinsic meniscus region.

### 2.2.1. Computational domain

The computational domain is a two-dimensional plane representing the shape of a liquid-vapor interface in an open capillary rectangular microchannel as depicted in Fig. 4. The interface profile is divided into two parts. The first part starts from  $x = 0$  and ends at  $x = x_{tf}$  corresponding to the thin-film region. This interface profile is obtained by the thin-film evaporation model described in Section 2.1. The second part starts from  $x = x_{tf}$  and extends towards the microchannel mid-line, indicating the intrinsic meniscus region, which is a constant curvature line. The interface profiles i.e., the function  $\delta(x)$  for both thin-film and intrinsic regions, are obtained by the thin-film evaporation model and exported from MATLAB to ANSYS Fluent and therefore, both regions are completely resolved by CFD simulation. Only half of the microchannel is modeled because of the symmetrical nature of the problem. Moreover, to reduce the effect of the inlet BC on the results, the computational domain is elongated in the  $x$  direction by half of the microchannel half-width as seen in Fig. 4.

### 2.2.2. Governing equations in CFD model

It is assumed that the flow is laminar, incompressible, and steady-state and the fluid has constant thermophysical properties as listed in Table 1. Then the continuity, momentum, and energy conservation equations are solved by ANSYS Fluent to obtain the velocity, pressure and temperature fields.

$$\rho_l \nabla \cdot \vec{V} = \dot{S}_m, \quad (16)$$

$$\rho_l \vec{V} \cdot \nabla \vec{V} = -\nabla p + \mu_l \nabla^2 \vec{V}, \quad (17)$$

$$\rho_l c_{p,l} \vec{V} \cdot \nabla (T) = k_l \nabla^2 T. \quad (18)$$

In the above formulae,  $\vec{V}$  and  $T$  are velocity vector and temperature, respectively. Moreover,  $\dot{S}_m$  is the source term in the continuity equation accounting for the evaporation mass flux from the interface. This source term is calculated by Eq. (19), and is only applied to the cells that are

adjacent to the interface using UDF programming in ANSYS Fluent.

$$\dot{S}_m = \dot{m}_{ev}^* \frac{A_{face}}{V_{cell}}. \quad (19)$$

In the above equation,  $\dot{m}_{ev}^*$  is the evaporation mass flux calculated by Eq. (11),  $A_{face}$  is the liquid-vapor interface area of the cell, and  $V_{cell}$  is the volume of the cell. It should be noted that  $P_d$  and  $P_c$  of each interface cell (those cells having one face placed on the liquid-vapor interface) are required to find  $\dot{m}_{ev}^*$  accurately. Therefore,  $P_d$  and  $P_c$  distributions, obtained by the thin-film evaporation model (Fig. 3), are exported to the ANSYS Fluent solver through UDF programming and interpolating techniques. It must be emphasized that the disjoining pressure  $P_d$  for the interface cells in the intrinsic meniscus region is set to zero while the capillary pressure  $P_c$  is set to a constant value obtained by thin-film evaporation model corresponding to the constant radius of curvature in this region.

Obtaining  $P_d$  and  $P_c$  pressure distributions as a function of length from the thin-film evaporation model and using UDF programming to feed them into the 2D CFD model enables the CFD simulation framework to simultaneously capture the micro-scale evaporation physics and macroscopic transport phenomena. In that way, the present work is somehow different from the previous research works which intended to incorporate the thermal characteristics of the micro region into the macroscopic CFD simulation such as in Refs. [30,31]. Here, the coupling between different length scales is achieved through implementation of some physics-capturing correlations, developed based on the numerical solution of the governing equation in the thin-film region, into the macroscopic CFD simulation. Therefore, in these works, the micro and macro region are not resolved simultaneously using a single CFD simulation setup.

Modeling the heat transfer associated with the evaporation from the interface can be implemented in two ways i.e., as a sink term in the energy conservation equation or as a boundary condition (interfacial heat transfer coefficient). The latter seems to be a better choice when considering the ease of implementation, faster convergence, and stability as suggested by previous researchers [36–38]. Therefore, this method is applied in which interfacial convection heat transfer coefficient  $h_{int}$  due to the local evaporation mass flux ( $\dot{m}_{ev}^*$ ) is given by:

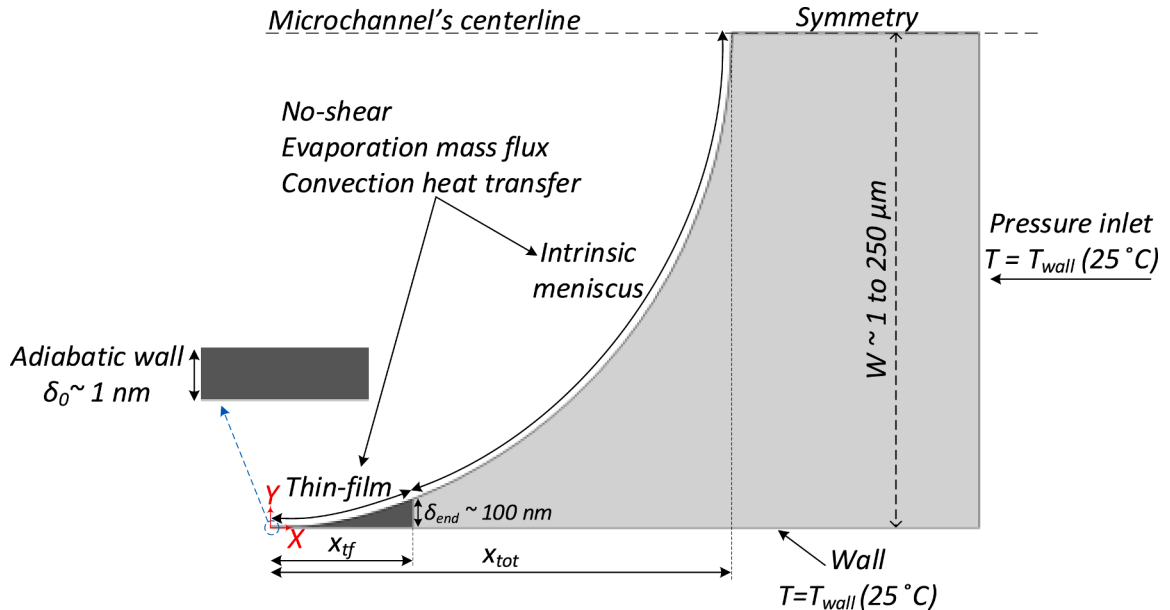


Fig. 4. Computational domain (extended meniscus) and boundary conditions.

$$h_{int} = \frac{\dot{m}_{evp} h_{fg}}{T_{int} - T_v}, \quad (20)$$

where, the free stream temperature for the convection heat transfer mechanism is the saturation vapor temperature  $T_v$ .

### 2.2.3. Boundary conditions

A pressure-inlet BC with a constant temperature being equal to the wall temperature ( $T_{wall}$ ) is imposed on the right-hand side of the domain as shown in Fig. 4. The adiabatic wall BC is considered for the beginning of the thin-film region at the left corner of the computational domain. The bottom wall is a constant temperature wall ( $T_{wall}$ ) with no-slip BC. A no-shear BC is applied on the interface along with an equivalent convection heat transfer coefficient,  $h_{int}$ , representing the heat transfer due to the evaporation as given by Eq. (20). The free-stream temperature is set equal to the vapor temperature i.e., 298.15 K. Furthermore, the disjoining and capillary pressure distributions at the interface are obtained through the thin-film evaporation model and fed into the 2D CFD model using UDF programming. As a result, the interface mass flux can be accurately calculated using Eq. (11).

### 2.2.4. Mesh generation

Quadrilateral mesh elements are generated for the whole computational domain. The element size in the thin-film region is of the order of 1 nm and it gradually increases until it reaches a value of less than 0.01 W in the intrinsic meniscus region, as represented in Fig. 5. The mesh study is performed in Section 3.2 to ensure that obtained results are mesh independent.

### 2.2.5. Solution algorithm

The thin-film profile calculated by the thin-film evaporation model along with the intrinsic meniscus profile, which is a constant curvature profile, is exported as a file to the CAD modeling software to create the 2D computational domain demonstrated in Section 2.2.1. Also, the pressure distributions (i.e.,  $P_d$  and  $P_c$ ) along the interface are taken from the thin-film evaporation model and given as an input file to ANSYS Fluent via UDF programming. The pressure distributions are required in order to accurately calculate the evaporation mass flux in Eqs. (19) and (11).

The coupled algorithm is used for pressure-velocity coupling. All governing equations are discretized by the second order upwind scheme. The solution is regarded as converged when all residuals fall below  $10^{-9}$  and the monitored values such as the inlet mass flow rate do not change further with increasing the number of iterations.

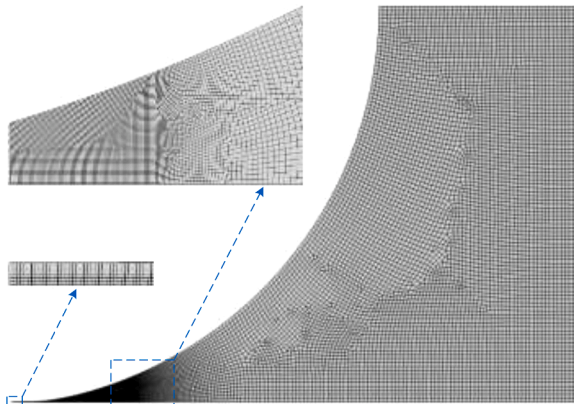


Fig. 5. Schematic representation of mesh elements.

## 3. Boundary condition, mesh, and validation studies

### 3.1. Boundary condition effects (thin-film model)

As mentioned in Section 2.1.1, the initial thickness of the thin-film region (or the adsorbed film thickness) needs to be higher than the value calculated by Eq. (13) so that a non-trivial solution can be obtained. Since there is no solid and consistent advice regarding how big the initial thickness of the thin-film region needs to be, it seems necessary to perform a preliminary analysis. Therefore, the variation of total heat transfer rate from the thin-film region along with the capillary pressure at the end of the thin-film region is monitored while the initial thickness used by the numerical model is varied from  $1.03 \times \delta_{0,formula}$  to  $2.0 \times \delta_{0,formula}$  as shown in Fig. 6. Here  $\delta_{0,formula}$  means the initial film thickness calculated by Eq. (13). It is seen that higher values of initial thickness lead to lower total heat transfer rates and a higher capillary pressure at the end. Therefore, one may simply conclude that lower factors ( $\delta_0/\delta_{0,formula}$ ) need to be used to reach a higher accuracy. However, as noticed by previous researchers [17,18,24], this factor has a significant impact on numerical stability and convergence. In other words, decreasing this factor results in a numerical solution that is highly sensitive to the first and second derivatives of the thin-film profile at zero ( $\delta'_0$  and  $\delta''_0$ ), especially at higher degrees of wall superheat. As a result, a lower factor necessitates choosing a smaller value for the length step in the Runge–Kutta method (as low as 0.01 nm) so that a convergent and stable solution could be established. However, such small length steps will be associated with a drastic increase in the solution's run-time. In consequence, the selection of this factor is a trade-off between accuracy and computational cost. Therefore, a factor of 1.2 is chosen in the present study to achieve both accuracy and convergence speed. It should be noted that the deviation between total heat transfer rates, calculated by a factor of 1.2 and 1.03, is less than 0.5 % for the case shown in Fig. 6, and this deviation reduces as the wall superheat increases.

As explained in Section 2.1.1, two different approaches can be adopted for determination of boundary conditions  $\delta'_0$  and  $\delta''_0$  as suggested by previous researchers. However, to the best of the author's knowledge, there is no study to compare these two approaches. Therefore, a case with  $W = 5.0 \mu\text{m}$  is considered to investigate how these two different BCs affect the results.

The total heat transfer rate from the thin-film region along with the length of the thin-film as a function of wall superheat is illustrated in Fig. 7. It can be deduced that the two different BCs have no appreciable impact on the results for the range of wall superheats considered in the present study. However, to better understand the effect of different BCs, the variation of capillary pressure and thin-film thickness along X axis are showcased in Fig. 8. The only difference between the two methods is related to the capillary pressure at the beginning of the thin-film region. For the first method in which  $\delta'_0 = 0$ , the capillary pressure is zero at  $x = 0$  and then it increases rapidly, but the capillary pressure is nonzero in the beginning for the second method ( $\delta''_0 = 0$ ). No considerable discrepancy can be observed between thin-film thickness profiles obtained by two different BC methods. Consequently, the first method is adopted in the present study because it is more appropriate in terms of convergence and ease of implementation in the thin-film evaporation model.

### 3.2. Mesh independence studies (CFD model)

To ensure that a mesh-independent solution is achieved, a preliminary survey is conducted by employing six different computational grids with varying degrees of refinement to quantify the effect of mesh resolution on the results. To this end, a global energy-related parameter and a local momentum-related parameter are considered i.e., the total heat transfer rate from extended meniscus ( $\dot{q}'_{tot}$ ) and the distribution of



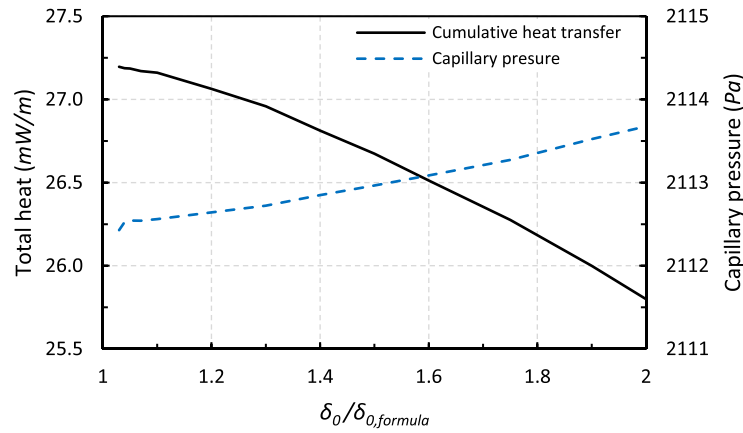


Fig. 6. Effect of initial film thickness on the total heat transfer rate from thin-film region and capillary pressure at the end of the thin-film region for  $W = 10.0 \mu\text{m}$  and  $\Delta T = 0.1 \text{ K}$ .

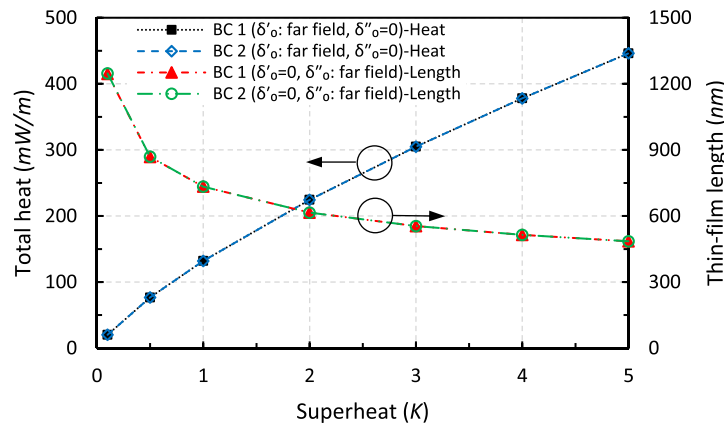


Fig. 7. Effect of boundary condition on the total heat transfer rate and thin-film length as a function of superheat for  $W = 5.0 \mu\text{m}$  (BC 1:  $\delta'_0$  is determined by far field condition and  $\delta''_0 = 0$ , BC 2:  $\delta'_0 = 0$  and  $\delta''_0$  is determined by far field condition).

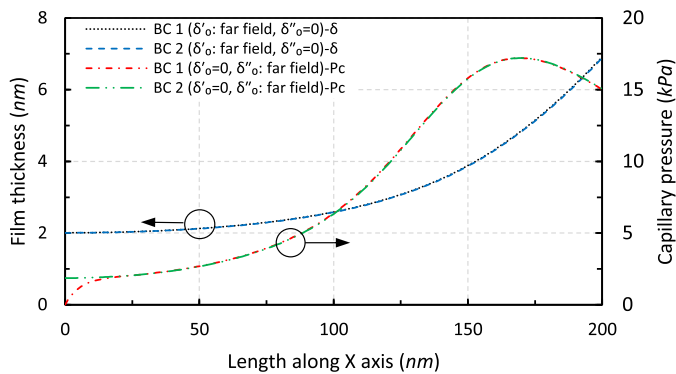


Fig. 8. Variation of film thickness and capillary pressure along X axis for  $W = 10 \mu\text{m}$  and  $\Delta T = 1.0 \text{ K}$  at two different boundary conditions (BC 1:  $\delta'_0$  is determined by far field condition and  $\delta''_0 = 0$ , BC 2:  $\delta'_0 = 0$  and  $\delta''_0$  is determined by far field condition).

interfacial velocity magnitude ( $V_{int}$ ).

The coarsest grid system (Mesh 1) has a total of 9141 elements while the finest one (Mesh 6) consists of 339,554 elements. The total rate of heat transfer from extended meniscus get larger as the number of mesh elements increases so that it finally reaches a constant value, see Fig. 9. Although the percentage difference between the finest and coarsest grid systems (Mesh 1 and Mesh 6) is less than 0.03 %, selected grid systems i.

e. Mesh 2, Mesh 4, and Mesh 6 are chosen to compare their influence on a local parameter i.e., interfacial velocity magnitude as depicted in Fig. 10. It should be noted that the interface velocity means the magnitude of liquid flow velocity at the liquid-vapor interface cells and therefore, it is parallel to the interface. Mesh 4 and Mesh 6 give identical interfacial velocity distribution while Mesh 2 underpredicts the velocity especially near the high velocity region i.e., around  $x = 75 \text{ nm}$ . As a result, Mesh 4 is chosen as the most appropriate grid system in terms of both accuracy and computational time.

### 3.3. CFD simulation validation

CFD simulation results are compared with thin-film evaporation model outputs to validate the 2D simulation framework. To this end, a rectangular capillary channel with  $W = 2.0 \mu\text{m}$  is modeled by the thin-film evaporation model explained in Section 2.1 and then the extended meniscus profile is exported to ANSYS Fluent as described in Section 2.2. The total heat transfer rates  $q_{tf}$  calculated by the thin-film evaporation model i.e., the evaporation mass flux from the liquid-vapor interface at the thin-film region times enthalpy of vaporization  $h_{fg}$ , at different wall superheats are compared with the total heat transfer rates obtained by the CFD simulation in Fig. 11. As can be observed, the deviation between the results i.e.,  $|q_{tf,m} - q_{tf,CFD}|/q_{tf,m}$ , is less than 0.07 % in all superheats, indicating that CFD simulation results are in very good agreement with the numerical thin-film modeling. Here  $q_{tf,m}$  and  $q_{tf,CFD}$  are the total heat transfer rates calculated by thin-film numerical

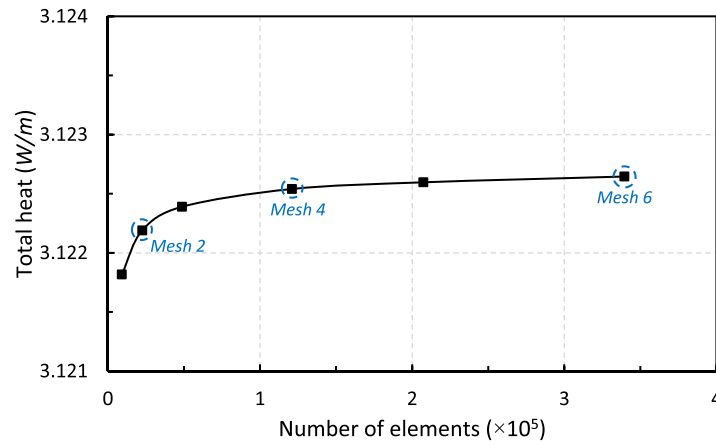


Fig. 9. Variation of total heat transfer rate from extended meniscus versus number of mesh elements ( $W = 10 \mu\text{m}$ ,  $\Delta T = 4.0 \text{ K}$ ).

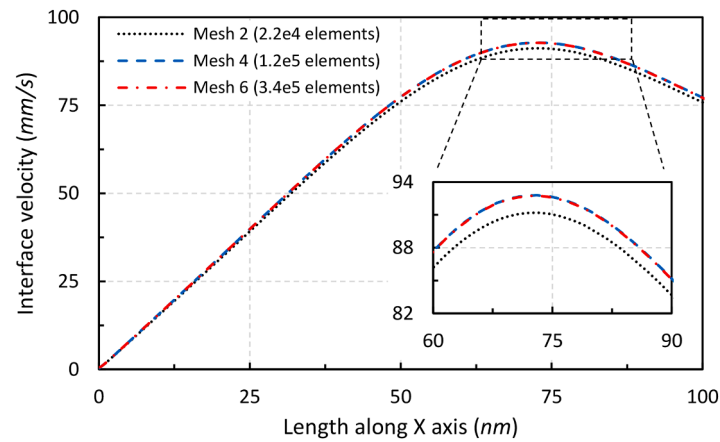


Fig. 10. Interface velocity distribution as a function of length for three different mesh sizes ( $W = 10 \mu\text{m}$ ,  $\Delta T = 4.0 \text{ K}$ ).

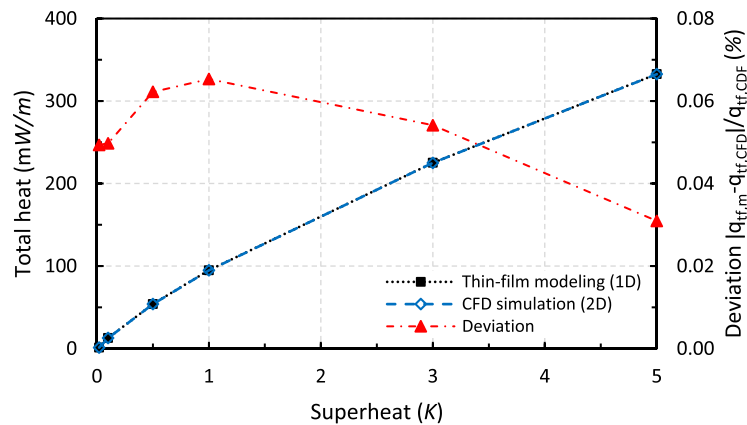


Fig. 11. Comparison of thin-film modeling and CFD simulation in terms of total heat transfer rate ( $W = 2.0 \mu\text{m}$ ).

modeling (Section 2.1) and CFD simulations (Section 2.2), respectively.

The variation of heat flux along the X-axis in the thin-film region for two different wall superheats is shown in Fig. 12. The results make it clear that there is no considerable distinction between thin-film modeling and CFD simulations in the thin-film region. Moreover, it proves that the fluid flow in the thin-film region is essentially unidirectional and transverse velocity effects are negligible, as it was concluded by Akkuş et al. [49] as well as Batzdorf et al. [54]. However, this is not the case for the intrinsic meniscus region.

#### 4. Results and discussion

The characteristics of thin-film evaporation in rectangular micro-channels covering a wide range of widths i.e.,  $W = 1\text{--}250 \mu\text{m}$ , are studied in this section using the thin-film evaporation model and the CFD simulation framework described in Sections 2.1 and 2.2, respectively. First, the effects of key parameters including channel width and wall superheat on the heat transfer characteristics of the thin-film region and extended meniscus are studied; then, several correlations are

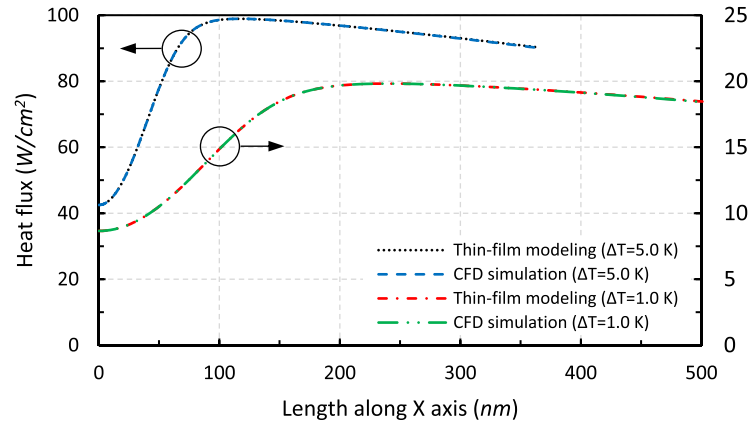


Fig. 12. Variation of heat flux along X axis in the thin-film region calculated by thin-film modeling and CFD simulation ( $W = 2.0 \mu\text{m}$ ).

developed based on the numerical simulation results.

Two thermal resistances including thin-film thermal resistance ( $R'_{tf}$ ) and total thermal resistance ( $R'_{tot}$ ) are defined as follows to support the presentation of the obtained results so that one can have a better view of the thermal characteristics of evaporation within microchannels.

$$R'_{tf} = \frac{(T_{wall} - T_v)}{\dot{m}'_{l,tf} h_{fg}}, \quad (21)$$

$$R'_{tot} = \frac{(T_{wall} - T_v)}{\dot{m}'_{l,tot} h_{fg}}, \quad (22)$$

In the above equations,  $\dot{m}'_{l,tf}$  and  $\dot{m}'_{l,tot}$  stand for evaporated liquid in the thin-film region and evaporated liquid in the extended meniscus, respectively. These thermal resistances along with interfacial convection heat transfer coefficient ( $h_{int}$ ), defined by Eq. (20), are used in the following sections.

#### 4.1. Comparison with previous data

As mentioned earlier, one of the main motives of performing 2D CFD simulation is to accurately determine the relative importance of evaporation heat flux from thin-film region compared to the evaporation from the extended meniscus. In this regard, Wang et al. [18] are one of the first researchers who performed numerical analyses to determine the characteristics of an evaporating thin-film and its total share in evaporation from an extended meniscus. They relied on the mathematical formulation developed for the thin-film region (see Section 2.1) to find the total heat transfer from the extended meniscus as well, like what was

done in several other studies [27,29]. In other words, they assumed that the mathematical formulation that was originally developed for analysis of thin-film evaporation in the thin-film region can also be used for the evaluation of evaporation heat transfer from the liquid-vapor interface in the intrinsic meniscus region. However, this does not seem to be an acceptable approach as will be discussed in the following paragraphs by considering two sets of numerical modeling performed based on the algorithm developed in Section 2.1.

First, we consider a rectangular microchannel with  $W = 2.5 \mu\text{m}$  and  $\Delta T = 1.0 \text{ K}$  modeled by the thin-film evaporation model and applying fluid properties given in Ref. [18]. Contrary to the normal conditions in which the thin-film evaporation model is interrupted at the end of the thin-film region (where Eq. (15) holds), now the numerical solution is extended towards the intrinsic meniscus region until it reaches the center of the microchannel. The film thickness profile, its slope (tangent of the first derivative), along with its radius of curvature ( $R^*$ ) are shown in Fig. 13. As it can be seen, the radius of curvature of the film increases in the thin-film region ( $x < \sim 200 \text{ nm}$ ) until it approaches an asymptotic value in the intrinsic meniscus region, indicating that the disjoining pressure effect has vanished and the interface shape is only governed by the capillary pressure. However, as observed in Fig. 13, this situation does not last until the end of the film profile. In fact, the radius of curvature increases sharply near the end of the film, where the film slope is approximately higher than  $75^\circ$ , violating the governing physics of the problem i.e., constant radius of curvature in the intrinsic meniscus region. This can be attributed to the simplifying assumption that was made for the thin-film region i.e., 1D fluid flow based on lubrication theory, which does not hold in the intrinsic meniscus region, especially for the higher film slopes near the center of the microchannel [55].

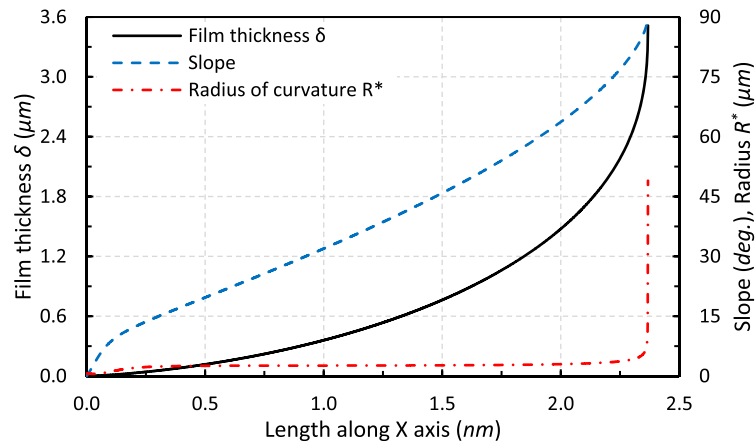


Fig. 13. Film thickness profile, slope, and radius of curvature for a microchannel with  $W = 2.5 \mu\text{m}$  and  $\Delta T = 1.0 \text{ K}$  (n-octane at  $70^\circ\text{C}$ ).

To elucidate the influence of the above-mentioned shortcoming on the numerical modeling outputs, the results obtained by Wang et al. [18] are compared with those calculated by the multi-scale modeling approach developed in the present study as indicated in Fig. 14. In this figure the percentage contribution of thin-film region to net heat transfer rate from extended meniscus has been given for a rectangular microchannel with  $W = 2.5 \mu\text{m}$  at different degrees of superheat. Obviously, the method presented by Wang et al. [18] significantly overpredicts the relative importance of heat transfer from the thin-film region at all superheats compared to that obtained by the present CFD model. Consequently, it can be concluded that the exact amount of evaporation heat flux from an extended meniscus in microchannels cannot be obtained by just performing thin-film evaporation analysis justifying the implementation of 2D CFD simulations.

#### 4.2. Thin-film length

As mentioned earlier, there is no well-established method to determine the thin-film region length. Some previous studies [18,46] have marked the end of the thin-film region as the location where the disjoining pressure drops to  $1/5000$ th of its value at  $x = 0$ . However, in the present study, a new definition is adopted to determine the end of the thin-film region as a point in which the ratio of disjoining pressure to capillary pressure becomes less than 0.001, as given by Eq. (15). The new definition is compared to the old one in Fig. 15, in which the variation of the disjoining and capillary pressures along the length of the thin-film region is depicted for two different channel sizes. As can be seen in Fig. 15(a) for a channel with  $W = 1 \mu\text{m}$ , the thin-film length calculated by the old definition is 660 nm, which is longer than the length given by the new definition (615 nm). Contrarily, for a large channel size of  $W = 100 \mu\text{m}$  shown in Fig. 15(b), the old definition finds that the thin-film length is 1504 nm, which is less than half of the value computed by the new definition i.e., 3525 nm.

Since the intrinsic meniscus region is defined as the region in which capillary forces dominate, it is expected that the meniscus curvature and capillary pressure remain constant in this region. However, based on information observed in Fig. 15, the intrinsic meniscus region predicted by the old definition ( $P_d = 1/5000 P_{d0}$ ) fails to comply with this requirement especially for larger channel sizes. Moreover, the old definition is solely dependent on the disjoining pressure and its initial value (which is in turn depends on  $\delta_0$  as given in Eq. (2)); therefore, it does not include the impact of capillary pressure and cannot be considered as a good indicator for the onset of the intrinsic meniscus. As a result, Eq. (15) is introduced as a better method for determining the end of the thin-film region and the beginning of the intrinsic meniscus.

The thin-film length variation with channel width and wall super-

heat is illustrated in Fig. 16. The results indicate that while a greater thin-film length is obtained for larger channels, the thin-film length reduces with an increase in the wall superheat. A higher wall superheat leads to a greater rate of liquid evaporation and therefore, a smaller thin-film length can be stabilized on the wall. To make it more clear how the thin-film region length reduces as the wall superheat increases, the variation of thin-film region length with wall superheat for a microchannel width of  $W = 50 \mu\text{m}$  is schematically shown in Fig. 17. As a result, thin-film length is a function of both channel width and wall superheat. These trends agree well with the numerical results reported by other researchers [18,19,34].

#### 4.3. Thin-film thickness

The thin-film thickness at the end of the thin-film region ( $\delta_{end}$ ) increases with channel width as shown in Fig. 18(a), ranging from about 50 nm to 350 nm. This is the consequence of the thin-film length definition given by Eq. (15). If one adopts the old definition for determining the thin-film length (i.e.,  $P_d = 1/5000 P_{d0}$ ), the thin-film thickness at the end will be insensitive to the channel width as given by Wang et al. [18]. Also, Fig. 18(a) indicates the capillary pressure at the end of the thin-film region (in other words, the constant capillary pressure in the intrinsic meniscus). It can be observed that the capillary pressure decreases monotonically with channel width, which is in accordance with the Young–Laplace equation (Eq. (3)), covering a wide range of values from about 21 kPa to less than 0.1 kPa. Furthermore, the changes in  $\delta_{end}$  with respect to wall superheat is shown in Fig. 18(b) for different channel sizes. It is obvious that changing the wall superheat does not have any influence on  $\delta_{end}$ , indicating that for a given channel width the onset of the intrinsic meniscus is the same for all wall superheats. In other words, no matter how much the wall superheat is, the intrinsic meniscus starts when the thin-film profile moves a constant distance ( $\delta_{end}$ ) away from the wall.

#### 4.4. Heat transfer characteristics

The local evaporation mass flux ( $\dot{m}_{evp}''$ ) and interfacial heat transfer coefficient ( $h_{int}$ ) are shown in Fig. 19 as a function of length along the X-axis. The local evaporation mass flux reaches its maximum value at a point located within the thin-film region, which is consistent with the observations of other researchers [17–20,22,24,43,44,49,55]. Also, the evaporation mass flux at  $x = 0$  is nonzero since, as mentioned in Section 2.1.1, a value slightly bigger than  $\delta_0$ , calculated by Eq. (13), is adopted to avoid the trivial solution. Another finding regarding Fig. 19 is that the interfacial heat transfer coefficient finds its maximum value within the thin-film region, as well. After the point of maximum, its trend depends

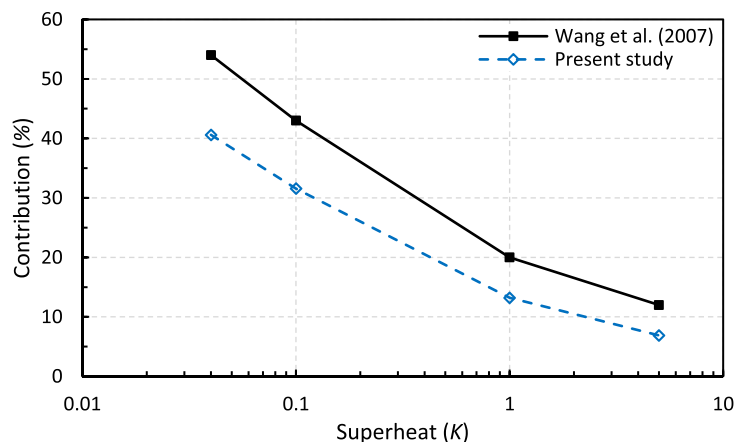


Fig. 14. Percentage contribution of thin-film region to net heat transfer rate for a microchannel with  $W = 2.5 \mu\text{m}$  and varying degrees of superheat (n-octane at  $70^\circ\text{C}$ ).

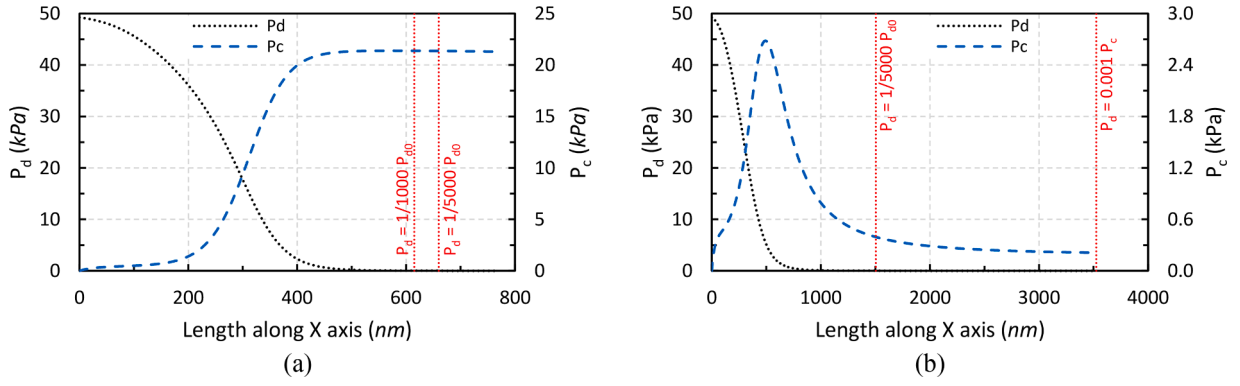


Fig. 15. Variation of the disjoining and capillary pressures along the X-axis together with different definitions for thin-film region length: (a)  $W = 1 \mu\text{m}$  and  $\Delta T = 0.1 \text{ K}$  and (b)  $W = 100 \mu\text{m}$  and  $\Delta T = 0.1 \text{ K}$ .

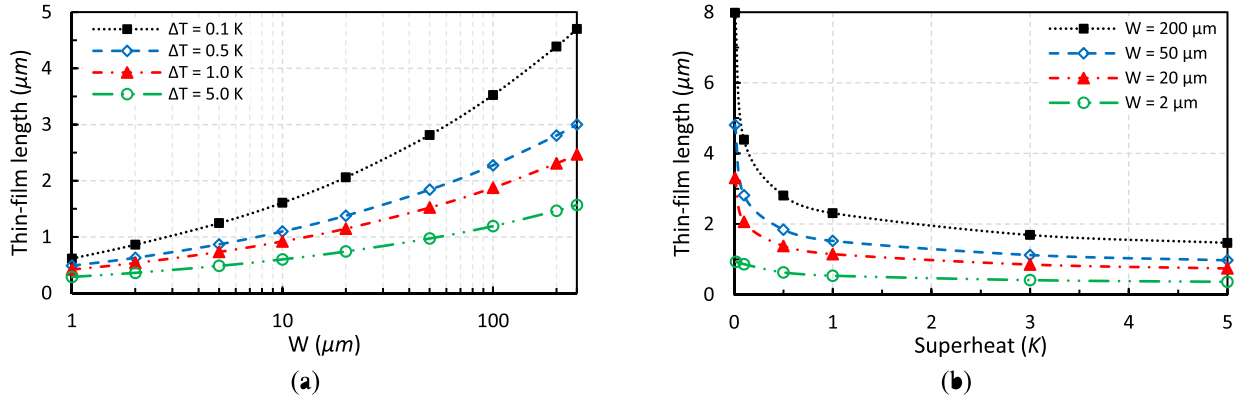


Fig. 16. Thin-film length: (a) as a function of channel width and (b) as a function of wall superheat.

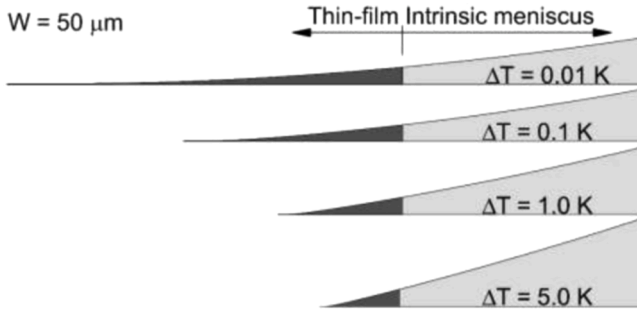


Fig. 17. Effect of wall superheat on the thin-film region length for  $W = 50 \mu\text{m}$ .

on the degree of superheat. For low superheats, as in Fig. 19(a),  $h_{int}$  decreases in the intrinsic meniscus while for high superheats, such as Fig. 19(b), it remains nearly constant all over the intrinsic meniscus.

Temperature contours for a microchannel with width of  $W = 5.0 \mu\text{m}$  and at two different wall superheats are presented in Fig. 20. It can be deduced that in the thin-film region the liquid temperature is very close to the wall temperature. In other words, the main reduction in the liquid temperature takes place in the intrinsic meniscus part of the domain. Therefore, one important conclusion is that the variation of fluid properties with temperature in the thin-film region can be neglected because of its fairly constant liquid temperature.

As expected, the rate of heat transfer from the thin-film region as well as the extended meniscus increases monotonically with both channel width and wall superheat as represented in Fig. 21. In fact, increasing the channel width results in a larger interfacial surface area, and consequently, a higher evaporation mass flux. Also, a larger temperature

difference between the wall and vapor improves the conduction heat transfer through the liquid, resulting in a higher rate of evaporation. Therefore, it would be beneficial to investigate the thin-film heat transfer characteristics based on the thermal resistances defined by Eqs. (21) and (22).

The variation of thin-film thermal resistance,  $R'_{tf}$ , and total thermal resistance,  $R'_{tot}$ , with channel width is plotted in Fig. 22 for different wall superheats. It can be observed that both thin-film and total thermal resistances decline versus the channel width. Moreover, while there is a significant distinction between thin-film thermal resistances at different wall superheats, this difference is less significant in case of total thermal resistance, as can be seen in Fig. 22(b). The total thermal resistance falls about one order of magnitude when the channel width changes from  $W = 1 \mu\text{m}$  to  $250 \mu\text{m}$  i.e., about two orders of magnitude. Furthermore, increasing the wall superheat leads to a higher thermal resistance (both  $R'_{tf}$  and  $R'_{tot}$ ) for all channel sizes except for small channel sizes at low superheats.

For a better understanding of thermal resistance behavior, the way that  $R'_{tf}$  and  $R'_{tot}$  change with regards to the wall superheat for a wide range of channel sizes are given in Fig. 23. For channel widths less than about  $W = 5 \mu\text{m}$ , a minimum point can be observed in thermal resistance graphs. This minimum point occurs where  $\Delta T$  is less than  $0.5 \text{ K}$ , and it is shifted towards lower superheats by increasing the channel width. When  $W$  is greater than  $5 \mu\text{m}$ , both  $R'_{tf}$  and  $R'_{tot}$  follow an increasing pattern and no minimum point can be observed in the charts. Therefore, it can be said that there is a turning point around  $W = 5 \mu\text{m}$ . For smaller channel sizes, when the wall superheat is less than about  $0.5 \text{ K}$ , the thermal resistance is strongly affected by the degree of wall superheat. In contrast, no matter what the channel size is, it can be found that the total



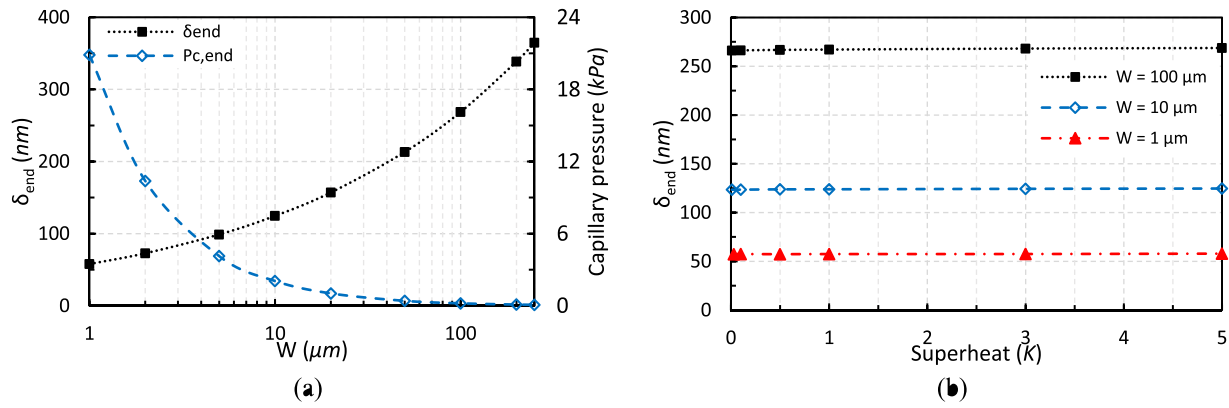


**Fig. 18.** (a) Thin-film thickness and capillary pressure at the end of thin-film region ( $\delta_{end}$  and  $P_{c,end}$ ) as a function of channel width for a constant wall superheat  $\Delta T = 5.0$  K and (b)  $\delta_{end}$  versus wall superheat for different channel sizes.

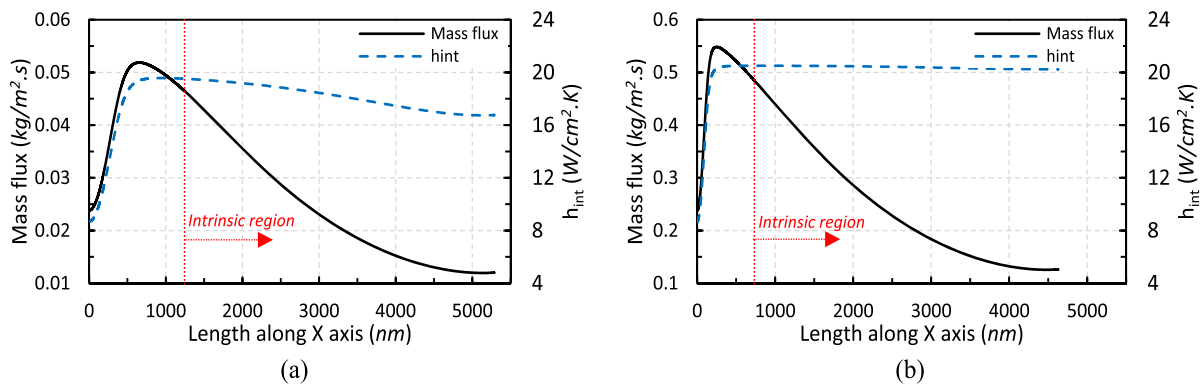


**Fig. 19.** Variation of mass flux and interfacial heat transfer coefficient along X axis for  $W = 5.0 \mu m$ : (a)  $\Delta T = 0.1$  K and (b)  $\Delta T = 1.0$  K.

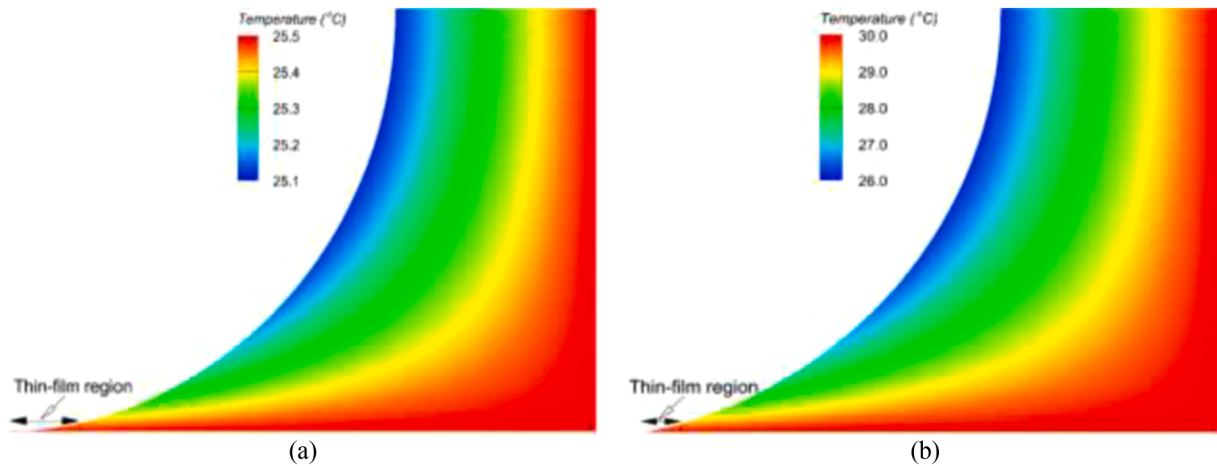


**Fig. 20.** Temperature contours for a channel width of  $W = 5.0 \mu m$ : (a)  $\Delta T = 0.5$  K and (b)  $\Delta T = 5.0$  K.

thermal resistance is a weak function of wall superheat when  $\Delta T$  is higher than about 0.5 K (Fig. 23(b)). These findings are used in the next section in order to develop proper correlations for the thin-film region and the total thermal resistances.

Another important result of the present study is the percentage contribution of the thin-film region to the total heat transfer rate from the extended meniscus. The percentage contributions are plotted in Fig. 24, representing a decreasing trend with respect to both channel width and wall superheat. The percentage contribution ranges from about 13 % to 38 % depending on the channel width and wall superheat,

indicating that the thin-film region plays a key role in evaporation from an extended meniscus. The importance of the thin-film evaporation heat transfer rate is nonnegligible even for large channel sizes simulated in the present study. Therefore, neglecting thin-film region as has been done in some previous studies [34–38,56] results in an inaccurate prediction of the heat transfer rate from an extended meniscus.

#### 4.5. Development of correlations

Thin-film evaporation is a micro-scale phenomenon that cannot be

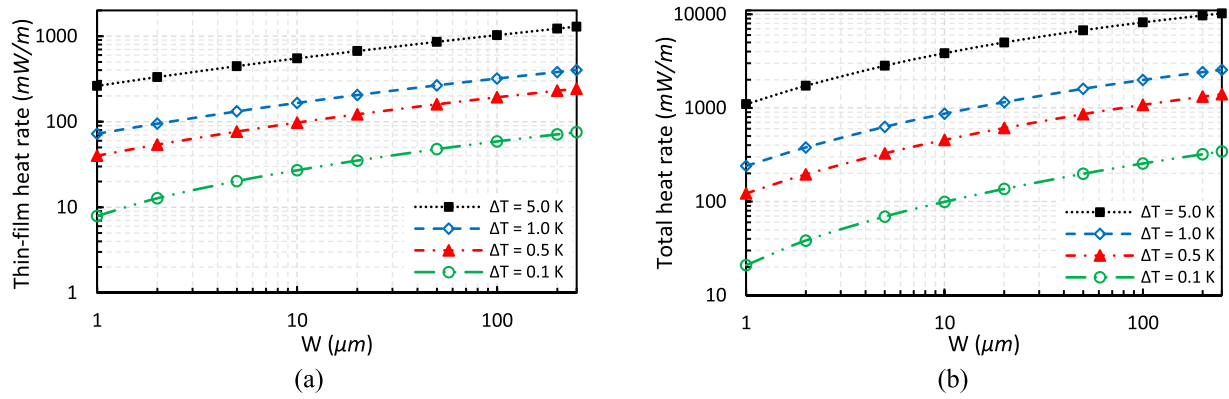


Fig. 21. Variation of heat transfer rate versus channel width for different degrees of wall superheat: (a) Thin-film heat transfer rate and (b) Total heat transfer rate.

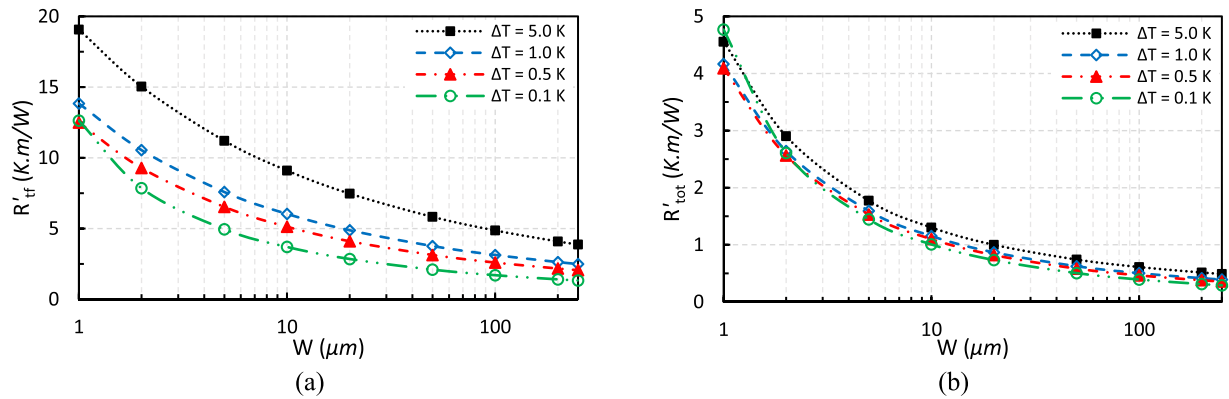


Fig. 22. Variation of thermal resistances with channel width for different degrees of wall superheat: (a) thin-film thermal resistance and (b) total thermal resistance.

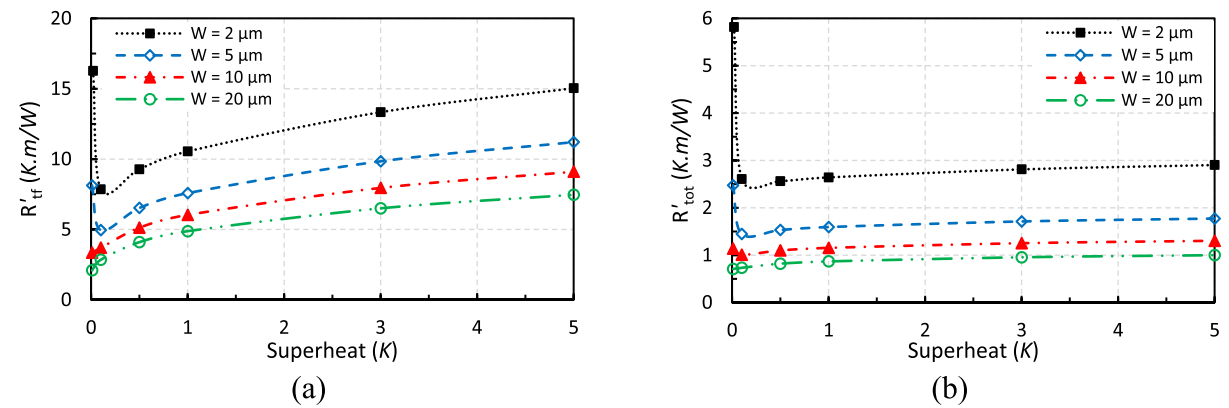


Fig. 23. Variation of thermal resistances with wall superheat for different channel widths: (a) thin-film thermal resistance and (b) total thermal resistance.

directly included in macro models such as a heat-pipe model. Therefore, one of the main objectives of the present study is to develop simple but accurate correlations to make a junction between micro-scale and macro-scale modeling. In fact, if it is intended to model the thermal characteristics of micro-sized devices, a multiscale approach needs to be adopted consisting of at least three parts i.e., a macro-scale model to calculate the system-level parameters, a micro-scale model to find the micro-level characteristics, and a junction model to make a junction between macro-scale and micro-scale models. However, the micro-scale model is not only difficult to be integrated with the macro-scale model, but also decreases the convergence speed of the model. Having these points in mind, it is found that establishing the total thermal resistance correlations based on 2D CFD simulation results will be an efficient

method for improving the flexibility and speed of mathematical models. In other words, using these simple thermal resistance correlations prevents the mathematical performance evaluation models from having to include both micro-scale model and junction model. In that sense, it could be said that the total thermal resistance correlations act like a bridge over micro-scale and macro-scale physics. As a result, multiple regression analysis is utilized to develop correlations for total thermal resistance based on the data points obtained by the numerical CFD simulations. The total thermal resistance correlations are of the following forms:

$$R'_{tot} \left[ \frac{K.m}{W} \right] = a_1 \Delta T^{a_2} \exp(a_3 \Delta T) W^{a_4} + a_5 \quad (23)$$

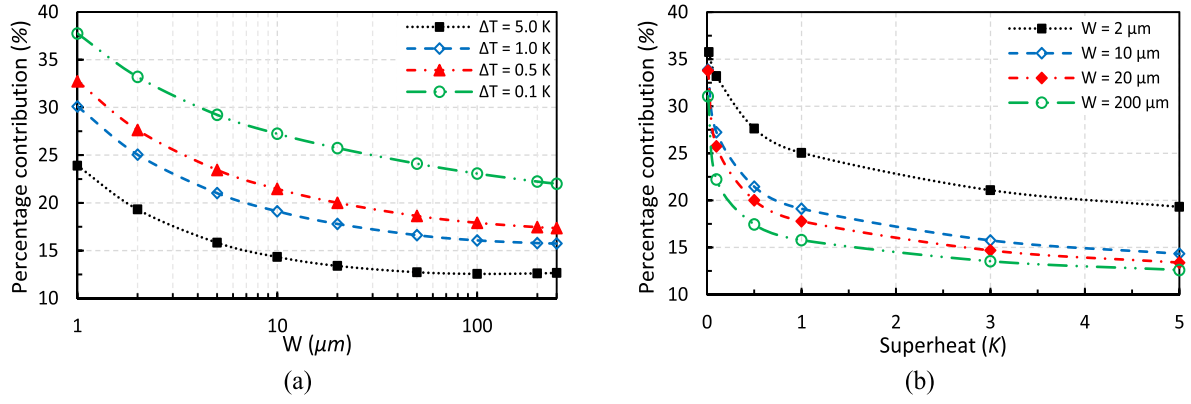


Fig. 24. Percentage contribution of thin-film region to total heat transfer as a function of: (a) channel width and (b) wall superheat.

$$R'_{tot} \left[ \frac{\text{K.m}}{W} \right] = \frac{\Delta T^{a_1} W^{a_2} + a_3}{\Delta T^{a_4} W^{a_5} + a_6} \quad (24)$$

In the above equations,  $\Delta T$  is the wall superheat in K, and  $W$  is the half of channel width in  $\mu\text{m}$ . Also,  $a_1$  to  $a_6$  are constants that are determined by regression analysis and can be found in Table 2. To increase the accuracy, the microchannel sizes are divided into two parts i.e.,  $1 \leq W (\mu\text{m}) < 5$  and  $5 \leq W (\mu\text{m}) \leq 250$ . Also, for the first part, the wall superheat range must be divided into two portions (i.e.,  $0.01 \leq \Delta T (\text{K}) < 0.05$  and  $0.05 \leq \Delta T (\text{K}) \leq 5.0$ ) in order to increase the curve fit accuracy. For the first portion, Eq. (23) gives the best results in terms of RMSE and average error while for the second portion Eq. (24) leads to better outputs. The coefficient of determination ( $R^2$ ) for all three developed correlations has an excellent value of 0.99. Also, the Root Mean Square Errors (RMSE) for the first and second portions of the first part ( $1 \leq W (\mu\text{m}) < 5$ ) are calculated to be 0.68 K.m/W and 0.14 K.m/W, respectively, and the value for the second part ( $5 \leq W (\mu\text{m}) \leq 250$ ) is just about 0.03 K.m/W indicating a good and acceptable fitting. Moreover, the average error of each developed correlation is less than 5 %. Therefore, it can be concluded that the developed correlations are able to predict the total thermal resistance with a high degree of accuracy.

A comparison has been made between output from these correlations and the numerical simulation results in Fig. 25. It can be seen that the total thermal resistances obtained by numerical simulations can be well fitted by Eqs. (23) and (24) and its corresponding constants given in Table 2. These correlations can be easily embedded into macro models to determine the evaporation heat flux or evaporation mass flux from a liquid-vapor meniscus with a high level of precision.

## 5. Conclusions

A numerical simulation framework is established in the present work to study the evaporation heat transfer mechanism from the extended meniscus formed in rectangular microchannels. The numerical model consists of two main parts: a thin-film evaporation model based on an

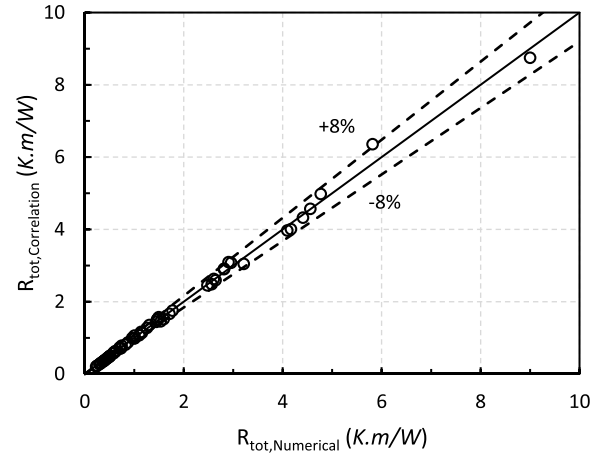


Fig. 25. Comparison of correlations outputs with numerical data for total thermal resistance.

augmented Young–Laplace equation, and a 2D CFD model for analyzing evaporation from the extended meniscus. The shape of the liquid-vapor interface is first obtained through the thin-film evaporation model. Then, the interface is exported to a CAD software to generate a 2D surface model. Afterwards, the grid structure is generated to prepare the model for performing CFD simulations. These simulations are based on a single-phase, steady, and laminar fluid flow model, and a series of user-defined functions (UDFs) are programmed to consider the effects of disjoining and capillary pressures on evaporation mass flux from the interface. The 2D model is then used to study the heat transfer characteristics of interfacial evaporation as well as to find three correlations for total thermal resistance. The most important findings of this study can be summarized as follows:

Table 2

Constants of curve fit along with fit characteristics.

Range	Equation	Fit data	$a_1$	$a_2$	$a_3$	$a_4$	$a_5$	$a_6$
$0.01 \leq \Delta T (\text{K}) < 0.05$ $1 \leq W (\mu\text{m}) < 5$	Eq. (23)	$R^2 = 0.999$ RMSE = 0.682 Avg. Error = 4.7 %	3103	0.6704	-88.86	-3.072	1.825	-
$0.05 \leq \Delta T (\text{K}) \leq 5.0$ $1 \leq W (\mu\text{m}) < 5$	Eq. (24)	$R^2 = 0.994$ RMSE = 0.141 Avg. Error = 3.0 %	0.337	-0.3465	0.0000	0.0743	0.0756	-0.7504
$0.01 \leq \Delta T (\text{K}) \leq 5.0$ $5 \leq W (\mu\text{m}) \leq 250$	Eq. (24)	$R^2 = 0.996$ RMSE = 0.034 Avg. Error = 3.5 %	0.2999	-0.1005	0.0058	0.1016	0.1488	-0.7062

- There is no considerable difference between thin-film profiles obtained by two different BC methods i.e., setting  $\delta'_0 = 0$  and finding  $\delta'_0$  by the far-field BC or setting  $\delta'_0 = 0$  and finding  $\delta'_0$  by the far-field BC. However, the first approach is recommended because of its better convergence and ease of implementation in the thin-film evaporation model.
- A new criterion is introduced to determine the thin-film length, which considers both disjoining and capillary pressures' impact i.e.,  $P_{d,end}/P_{c,end} < 10^{-3}$ . This criterion can accurately predict the onset of the intrinsic meniscus for different channel sizes and wall superheats.
- It is shown that the thin-film evaporation model is not capable of calculating the exact amount of evaporation mass flux from an extended meniscus. In other words, it fails to give reasonable results for the end parts of the meniscus near the centerline of the micro-channel. Therefore, the utilization of a 2D CFD simulation is justified to overcome this shortcoming.
- Based on the thin-film evaporation model and the new criterion defined for thin-film length, it is found that the thin-film thickness at the end of the thin-film region ( $\delta_{end}$ ) is just a function of channel width and not the wall superheat.
- While the heat transfer rate from the thin-film region and extended meniscus ( $\dot{q}'_{tf}$  and  $\dot{q}'_{tot}$ , respectively) increases with the channel width and wall superheat, the thermal resistance of thin-film and extended meniscus regions ( $R'_{tf}$  and  $R'_{tot}$ ) are decreasing functions of channel width. However, the variation of the thermal resistances with wall superheat is not monotonic. Indeed, they have a minimum point observed at superheats less than 0.5 K when the channel width is less than about  $W = 5 \mu\text{m}$ .
- The thin-film region has a significant contribution in the total heat transfer from the extended meniscus which is calculated to be between 13 % and 38 % for the range of parameters included in the

present study. The percentage contribution becomes larger when the channel width or wall superheat decreases.

- Using multiple regression analysis based on the obtained 2D CFD simulation results, three correlations are developed for the calculation of the total thermal resistance. These correlations are useful tools that can be easily included in the macro-models as boundary conditions.

#### CRediT authorship contribution statement

**Ali Mostafazade Abolmaali:** Conceptualization, Data curation, Formal analysis, Investigation, Methodology, Validation, Writing – original draft, Writing – review & editing. **Mohamad Bayat:** Conceptualization, Funding acquisition, Project administration, Supervision. **Jesper Hattel:** Conceptualization, Funding acquisition, Project administration, Supervision, Writing – review & editing.

#### Declaration of Competing Interest

The authors have no conflicts of interest to declare.

#### Data availability

Data will be made available on request.

#### Acknowledgments

The authors received funding from Independent Research Fund Denmark, DFF-FP2 DIGI-3D projects (Contract No. 0136-00210B) and Extreme heat (Contract No. 2035-00193B).

## Appendix A

### Derivation of the gradient of liquid mass flow rate

To find the relation between liquid mass flow rate  $\dot{m}'_l$  and the evaporative mass flux  $\dot{m}'_{evp}$  in the extended meniscus region, a representative liquid element as shown in Fig. A.1 is used. The mass balance equation is as follows:

$$\dot{m}'_l - (\dot{m}'_l + d\dot{m}'_l) - \dot{m}'_{evp} \frac{dx}{\cos\alpha} = 0 \Rightarrow \frac{d\dot{m}'_l}{dx} = -\frac{\dot{m}'_{evp}}{\cos\alpha}. \quad (\text{A.1})$$

In the above equation,  $\alpha$  is the interface angle of the liquid element which can be related to the slope of the interface profile  $\delta$  by the following formula:

$$\frac{1}{\cos\alpha} = \sqrt{1 + \tan^2\alpha} \xrightarrow{\tan\alpha=\delta} \frac{1}{\cos\alpha} = \sqrt{1 + \delta^2} \quad (\text{A.2})$$

By substituting Eq. (A.2) into Eq. (A.1), Eq. (8) is obtained relating the gradient of liquid mass flow rate to the evaporative mass flux and the slope of the interface profile.

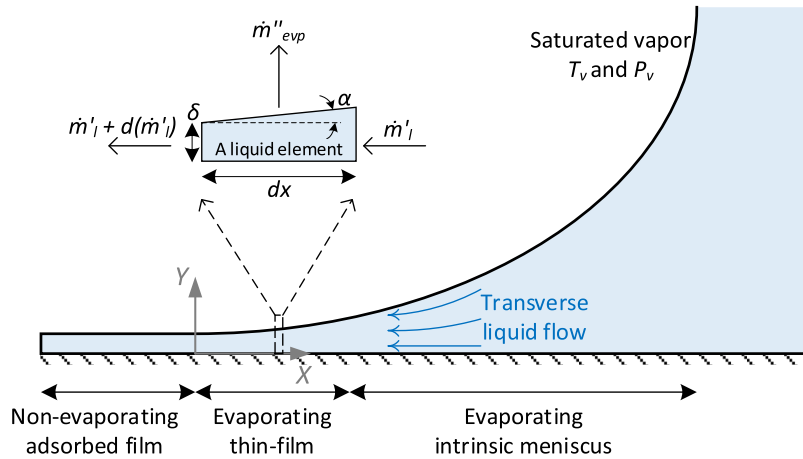


Fig. A.1. A representative element of liquid in the extended meniscus region with its associated mass fluxes.

## Appendix B

### Derivation of the far-field boundary condition

In the case of a rectangular microchannel such as that shown in Fig. B.1, the far-field boundary condition means that the radius of curvature at the end of the thin-film region  $R_{end}$ , where  $P_{d,end}/P_{c,end} < 10^{-3}$  (see Eq. (15)), should be equal to the curvature of the intrinsic meniscus region. Also, it is assumed that the intrinsic meniscus region can be approximated by an arc of a circle with its center located on the microchannel's centerline as depicted in Fig. B.1. Therefore, the following relation between the geometrical parameters must be satisfied to fulfill the far-field boundary condition:

$$W = \delta_{end} + R_{end} \cos \alpha. \quad (B.1)$$

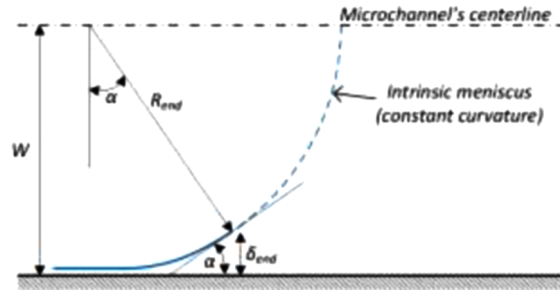


Fig. B.1. Schematic representation of the extended meniscus in a microchannel with details of the intersection point between thin-film and intrinsic meniscus regions.

In the above equation,  $\delta_{end}$  and  $\alpha$  are the thin-film thickness and the interface angle at the end of the thin-film region (i.e., the intersection of thin-film and intrinsic meniscus regions), respectively. The curvature radius at the end of the thin-film region  $R_{end}$  can be related to the first and second derivatives of the thin-film profile as below:

$$R_{end} = \frac{(1 + \delta_{end}^{'2})^{1.5}}{\delta_{end}''}. \quad (B.2)$$

By substituting Eq. (B.2) into Eq. (B.1) and using Eq. (A.1) to replace  $\cos \alpha$  by  $(1 + \delta_{end}^{'2})^{-0.5}$ , the following far-field boundary condition is obtained:

$$W = \delta_{end} + \frac{(1 + \delta_{end}^{'2})^{1.5}}{\delta_{end}''} (1 + \delta_{end}^{'2})^{-0.5} \Rightarrow W = \delta_{end} + \frac{1 + \delta_{end}^{'2}}{\delta_{end}''}. \quad (B.3)$$

## References

- [1] L. He, X. Tang, Q. Luo, Y. Liao, X. Luo, J. Liu, L. Ma, D. Dong, Y. Gan, Y. Li, Structure optimization of a heat pipe-cooling battery thermal management system based on fuzzy grey relational analysis, *Int. J. Heat Mass Transf.* 182 (2022), 121924, <https://doi.org/10.1016/j.ijheatmasstransfer.2021.121924>.
- [2] Y. Wang, D. Dan, Y. Zhang, Y. Qian, S. Panchal, M. Fowler, W. Li, M.K. Tran, Y. Xie, A novel heat dissipation structure based on flat heat pipe for battery thermal management system, *Int. J. Energy Res.* 46 (2022) 15961–15980, <https://doi.org/10.1002/er.8294>.
- [3] A. Wei, J. Qu, H. Qiu, C. Wang, G. Cao, Heat transfer characteristics of plug-in oscillating heat pipe with binary-fluid mixtures for electric vehicle battery thermal management, *Int. J. Heat Mass Transf.* 135 (2019) 746–760, <https://doi.org/10.1016/j.ijheatmasstransfer.2019.02.021>.
- [4] M. Levêque, S. Dutour, Investigation of the dynamics of a capillary pumped loop assisted with a mechanical pump: influence of pump location, *Appl. Therm. Eng.* 221 (2023), 119854.



- [5] M. Khalili, A. Mostafazade Abolmaali, M.B. Shafii, Experimental and analytical study of thermohydraulic performance of a novel loop heat pipe with an innovative active temperature control method, *Appl. Therm. Eng.* (2018) 143, <https://doi.org/10.1016/j.applthermaleng.2018.08.008>.
- [6] K. Zeghari, H. Louahlia, Flat miniature heat pipe with sintered porous wick structure: experimental and mathematical studies, *Int. J. Heat Mass Transf.* 158 (2020), 120021.
- [7] G. Wang, Z. Quan, Y. Zhao, H. Wang, Effect of geometries on the heat transfer characteristics of flat-plate micro heat pipes, *Appl. Therm. Eng.* 180 (2020), 115796.
- [8] A. Faghri, *Heat Pipe Science and Technology*, Global Digital Press, 1995.
- [9] L. Bai, G. Lin, G.P. Peterson, Evaporative heat transfer analysis of a heat pipe with hybrid axial groove, *J. Heat Transf.* 135 (2013) 31503.
- [10] H. Alijani, B. Çetin, Y. Akkuş, Z. Dursunkaya, Effect of design and operating parameters on the thermal performance of aluminum flat grooved heat pipes, *Appl. Therm. Eng.* 132 (2018) 174–187.
- [11] P.C. Stephan, C.A. Busse, Assessment of an improved model for the heat transfer coefficient of grooved heat pipe evaporators, *ESA Spec. Publ.* 1 (1991) 587–592.
- [12] B.V. Derjaguin, S.V. Nerpin, N.V. Churaev, Effect of film transfer upon evaporation of liquids from capillaries, *Bull. Rilem.* 29 (1965) 93–98.
- [13] P.C. Wayner Jr., C.L. Coccio, Heat and mass transfer in the vicinity of the triple interline of a meniscus, *AIChE J.* 17 (1971) 569–574.
- [14] M. Potash Jr, P.C. Wayner Jr, Evaporation from a two-dimensional extended meniscus, *Int. J. Heat Mass Transf.* 15 (1972) 1851–1863.
- [15] P.C. Wayner Jr, Y.K. Kao, L.V. LaCroix, The interline heat-transfer coefficient of an evaporating wetting film, *Int. J. Heat Mass Transf.* 19 (1976) 487–492.
- [16] P.C. Wayner Jr, The effect of interfacial mass transport on flow in thin liquid films, *Colloids Surf.* 52 (1991) 71–84.
- [17] S.-Y. Du, Y.-H. Zhao, New boundary conditions for the evaporating thin-film model in a rectangular micro channel, *Int. J. Heat Mass Transf.* 54 (2011) 3694–3701.
- [18] H. Wang, S.V. Garimella, J.Y. Murthy, Characteristics of an evaporating thin film in a microchannel, *Int. J. Heat Mass Transf.* 50 (2007) 3933–3942.
- [19] P.C. Stephan, C.A. Busse, Analysis of the heat transfer coefficient of grooved heat pipe evaporator walls, *Int. J. Heat Mass Transf.* 35 (1992) 383–391.
- [20] J.M. Ha, G.P. Peterson, The interline heat transfer of evaporating thin films along a micro grooved surface, (1996).
- [21] K. Bellur, E.F. Médici, C.K. Choi, J.C. Hermanson, J.S. Allen, Multiscale approach to model steady meniscus evaporation in a wetting fluid, *Phys. Rev. Fluids.* 5 (2020) 24001.
- [22] R. Bertossi, Z. Lataoui, V. Ayel, C. Romestant, Y. Bertin, Modeling of thin liquid film in grooved heat pipes, *Numer. Heat Transf. Part A Appl.* 55 (2009) 1075–1095.
- [23] J.-J. Zhao, M. Huang, Q. Min, D.M. Christopher, Y.-Y. Duan, Near-wall liquid layering, velocity slip, and solid–liquid interfacial thermal resistance for thin-film evaporation in microchannels, *Nanoscale Microscale Thermophys. Eng.* 15 (2011) 105–122.
- [24] M.S. Hanchak, M.D. Vangsness, L.W. Byrd, J.S. Ervin, Thin film evaporation of n-octane on silicon: experiments and theory, *Int. J. Heat Mass Transf.* 75 (2014) 196–206.
- [25] Y. Akkuş, Z. Dursunkaya, A new approach to thin film evaporation modeling, *Int. J. Heat Mass Transf.* 101 (2016) 742–748.
- [26] E. Lim, Y.M. Hung, B.T. Tan, A hydrodynamic analysis of thermocapillary convection in evaporating thin liquid films, *Int. J. Heat Mass Transf.* 108 (2017) 1103–1114.
- [27] R. Mandel, A. Shoostari, M. Ohadi, Thin-film evaporation on microgrooved heatsinks, *Numer. Heat Transf. Part A Appl.* 71 (2017) 111–127.
- [28] B. Fu, N. Zhao, B. Tian, W. Corey, H. Ma, Evaporation heat transfer in thin-film region with bulk vapor flow effect, *J. Heat Transf.* 140 (2018) 11502.
- [29] J. VS, A. Ambirajan, A.A. Adoni, J.H. Arakeri, Numerical investigation of an evaporating meniscus in a heated capillary slot, *Heat Mass Transf.* 55 (2019) 3675–3688.
- [30] S. Herbert, S. Fischer, T. Gambaryan-Roisman, P. Stephan, Local heat transfer and phase change phenomena during single drop impingement on a hot surface, *Int. J. Heat Mass Transf.* 61 (2013) 605–614.
- [31] C. Kunkelmann, P. Stephan, CFD simulation of boiling flows using the volume-of-fluid method within OpenFOAM, *Numer. Heat Transf. Part A Appl.* 56 (2009) 631–646.
- [32] G. Son, V.K. Dhir, Numerical simulation of nucleate boiling on a horizontal surface at high heat fluxes, *Int. J. Heat Mass Transf.* 51 (2008) 2566–2582.
- [33] K.H. Do, S.J. Kim, S.V. Garimella, A mathematical model for analyzing the thermal characteristics of a flat micro heat pipe with a grooved wick, *Int. J. Heat Mass Transf.* 51 (2008) 4637–4650.
- [34] R. Ranjan, J.Y. Murthy, S.V. Garimella, Analysis of the wicking and thin-film evaporation characteristics of microstructures, (2009).
- [35] R. Ranjan, J.Y. Murthy, S.V. Garimella, U. Vadakkan, A numerical model for transport in flat heat pipes considering wick microstructure effects, *Int. J. Heat Mass Transf.* 54 (2011) 153–168.
- [36] R. Ranjan, J.Y. Murthy, S.V. Garimella, A microscale model for thin-film evaporation in capillary wick structures, *Int. J. Heat Mass Transf.* 54 (2011) 169–179.
- [37] K.K. Bodla, J.Y. Murthy, S.V. Garimella, Evaporation analysis in sintered wick microstructures, *Int. J. Heat Mass Transf.* 61 (2013) 729–741.
- [38] K.S. Remella, F.M. Gerner, Thin-film evaporation in a mesh screen wick, *J. Heat Transf.* 144 (2022), 111601.
- [39] X. Wang, Y. Li, J.A. Malen, A.J.H. McGaughey, Assessing the impact of disjoining pressure on thin-film evaporation with atomistic simulation and kinetic theory, *Appl. Phys. Lett.* 116 (2020) 213701.
- [40] D. Khurstalev, A. Faghri, Heat transfer during evaporation on capillary- grooved structures of heat pipes, *J. Heat Transf.* 117 (1995) 740–747, <https://doi.org/10.1115/1.2822638>.
- [41] V. Sartre, M.C. Zaghdoudi, M. Lallemand, Effect of interfacial phenomena on evaporative heat transfer in micro heat pipes 1, *Int. J. Therm. Sci.* 39 (2000) 498–504, [https://doi.org/10.1016/S1290-0729\(00\)00205-2](https://doi.org/10.1016/S1290-0729(00)00205-2).
- [42] S.K. Wee, K.D. Kihm, K.P. Hallinan, Effects of the liquid polarity and the wall slip on the heat and mass transport characteristics of the micro-scale evaporating transition film, *Int. J. Heat Mass Transf.* 48 (2005) 265–278, <https://doi.org/10.1016/j.ijheatmasstransfer.2004.08.021>.
- [43] J. Zhao, X. Peng, Y. Duan, Slip and micro flow characteristics near a wall of evaporating thin films in a micro channel, *Heat Transf. Res.* 39 (2010) 460–474.
- [44] L. Biswal, S.K. Som, S. Chakraborty, Thin film evaporation in microchannels with slope- and curvature-dependent disjoining pressure, *Int. J. Heat Mass Transf.* 57 (2013) 402–410.
- [45] Z.-H. Kou, H.-T. Lv, W. Zeng, M.-L. Bai, J.-Z. Lv, Comparison of different analytical models for heat and mass transfer characteristics of an evaporating meniscus in a micro-channel, *Int. Commun. Heat Mass Transf.* 63 (2015) 49–53.
- [46] S. Ahmed, M. Pandey, New insights on modeling of evaporation phenomena in thin films, *Phys. Fluids* 31 (9) (2019).
- [47] R.W. Schrage, *A Theoretical Study of Interphase Mass Transfer*, Columbia University Press, 1953.
- [48] V.P. Carey, *Liquid-Vapor Phase-Change Phenomena: An Introduction to the Thermophysics of Vaporization and Condensation Processes in Heat Transfer Equipment*, CRC Press, 2020.
- [49] Y. Akkuş, H.I. Tarman, B. Çetin, Z. Dursunkaya, Two-dimensional computational modeling of thin film evaporation, *Int. J. Therm. Sci.* 121 (2017) 237–248.
- [50] H.B. Ma, G.P. Peterson, Temperature variation and heat transfer in triangular grooves with an evaporating film, *J. Thermophys. Heat Transf.* 11 (1997) 90–97.
- [51] C. Yan, H.B. Ma, Analytical solutions of heat transfer and film thickness in thin-film evaporation, *J. Heat Transf.* 135 (2013) 31501.
- [52] A.J. Shkarah, M.Y. Bin Sulaiman, M.R. bin Hj Ayob, Analytical solutions of heat transfer and film thickness with slip condition effect in thin-film evaporation for two-phase flow in microchannel, *Math. Probl. Eng.* 2015 (2015) 369581.
- [53] J.-J. Zhao, Y.-Y. Duan, X.-D. Wang, B.-X. Wang, Effects of superheat and temperature-dependent thermophysical properties on evaporating thin liquid films in microchannels, *Int. J. Heat Mass Transf.* 54 (2011) 1259–1267.
- [54] S. Batzdorf, T. Gambaryan-Roisman, P. Stephan, Direct numerical simulation of the microscale fluid flow and heat transfer in the three-phase contact line region during evaporation, *J. Heat Transf.* 140 (2018) 32401.
- [55] V.S. Ajaev, O.A. Kabov, Heat and mass transfer near contact lines on heated surfaces, *Int. J. Heat Mass Transf.* 108 (2017) 918–932.
- [56] A. Wei, X. Ren, S. Lin, X. Zhang, CFD analysis on flow and heat transfer mechanism of a microchannel  $\Omega$ -shape heat pipe under zero gravity condition, *Int. J. Heat Mass Transf.* 163 (2020), 120448.